Study of Li-Ion Conducting Polymer- Inorganic Composite Materials

March　２０１９

Shintaro Kitajima

Study of Li-Ion Conducting Polymer- Inorganic Composite Materials

Graduate School of Systems and Information Engineering

University of Tsukuba

March ２０１９

Shintaro Kitajima

Abstract

Solid-state lithium-ion conductors are attractive materials for next-generation secondary batteries owing to their advantages such as high energy density, compactness, and safety. However, their practical application faces several resistive issues. Thus, the interpretations of the lithium-ion transporting mechanism as well as the development of solid-state lithium-ion conductors are required for the successful practical application of solid-state lithium-ion conductors.

This dissertation presents the designed novel polymer/inorganic composite materials, where inorganic ion conductive particles are embedded as a single layer in the polymer matrix. The lithium-ion transfer mechanisms of these designed composite materials are carefully investigated via AC impedance spectroscopy. These composite materials exhibit surprisingly higher ionic conductivities and considerably lower activation energies than the commercial and sintered inorganic ion conductors because of the fast ion-transport pathways. Furthermore, the processing of the composite materials is discussed and a method to control the factors related to ionic conductivity is demonstrated. Finally, the battery characteristics in using the composite materials in batteries as well as the phenomena of lithium dendrite suppression in terms of lithium metal usage are discussed to express the possibilities of application to the batteries. These approaches result in the implementation of new opportunities for composite materials to be used in practical applications, including in all-solid-state lithium-ion batteries.

1

Contents

3

1   Introduction

1.1   Secondary batteries for electric vehicles

Compared to gasoline-fuelled conventional vehicles, electric vehicles, such as hybrid electric vehicles (HEVs), plug-in hybrid electric vehicle (PHEVs), and especially, all-electric vehicles (EVs) have much less or even zero tailpipe emissions, which can significantly reduce the amount of greenhouse gases and air pollutants. One of the core technologies of electric vehicles is the secondary batteries.

In the 1970s, lithium (Li) batteries were initially suggested by M. S. Whittingham [1]. Then, in the 1980s, important succeeds of lithium-ion batteries (LIBs) were achieved by Akira Yoshino, John B. Goodenough, and others [2]. LIBs were initially released by Sony in 1991 and, since then, considerable R&D has been conducted. Although, nowadays, the current-state LIBs can be seen everywhere and every time and the market of LIBs is gradually expanding, from micro electrochemical systems to portable electronics, and then to electrified vehicles and/or huge energy storage systems. Meanwhile, the demand for lighter and safer rechargeable batteries has been growing [3-5].

1.2   Post lithium-ion batteries

Currently the well-noteworthy post LIBs are lithium sulfur (Li-S) batteries, lithium-oxygen (Li-O$_2$) batteries and all-solid-state LIBs. Fig. 1-1 shows a Ragone plot among various secondary batteries [6]. This plot demonstrates that the theoretical potential

abilities of the candidates of the post LIBs.

Li-S batteries and Li-O$_2$ batteries have been proposed to meet the demand of the lighter battery. These batteries potentially promise significant increases of the energy density due to the use of lightweight elements of sulfur and oxygen as cathode materials, respectively. Li-S batteries remain significant challenges: low electrical conductivity and high volume expansion on lithiation and the shuttle effect of polysulfide [7-9]. Li-O$_2$ batteries suffer from the decomposition of electrolytes and electrode materials. These problems of Li-S batteries and Li-O$_2$ batteries result in poor cyclability, low efficiencies and poor rate capability [10, 11]. Thus, Li-S and Li-O$_2$ batteries are under intense investigation.

Fig. 1-1. Ragone plots among various secondary batteries [6].
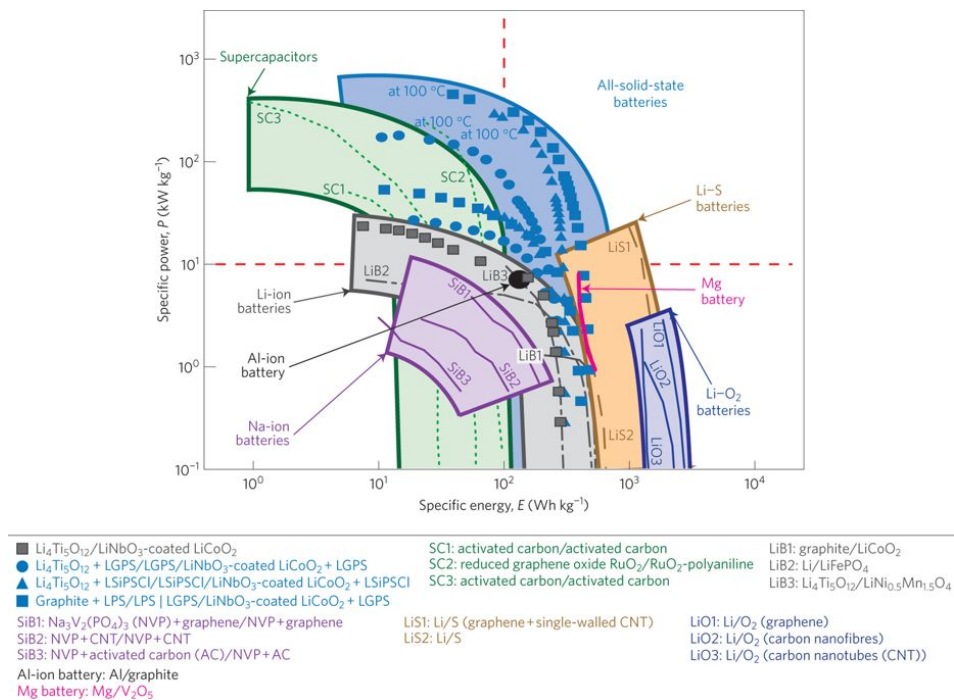
On the other hand, the demand of the safer battery will be fulfilled by the realization of all-solid-state LIBs. In conventional LIBs, there are risks of explosion or fire because of the low thermal stability and low flame point of organic liquid electrolytes. Owing to this issue, all-solid-state LIBs have been suggested as a promising fundamental solution [12-14].
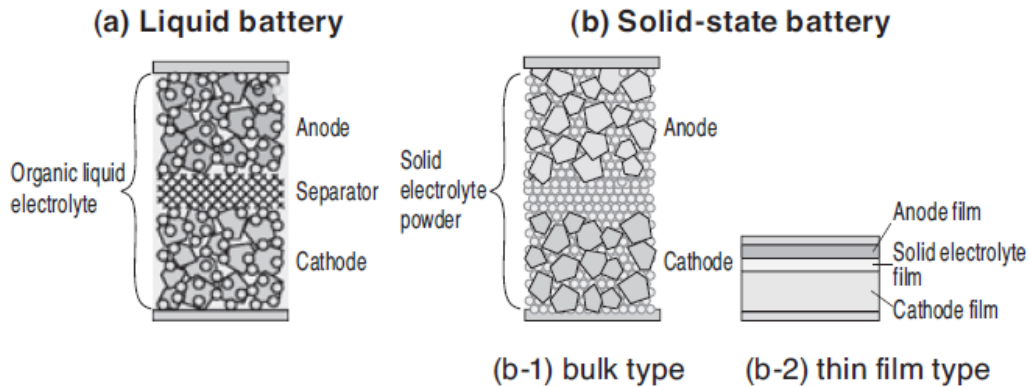
Fig. 1-2. Typical schematic cross-sectional views of (a) a liquid battery in conventional LIBs and (b) all-solid-state LIBs [15]

1.3   All solid-state batteries and motivation

All-solid-state LIBs are batteries in which the liquid electrolytes of conventional LIBs are replaced with solid electrolytes as shown in Fig. 1-2. The fire and explosion risks can be avoided or decreased by using the flame-retardant solid electrolytes. This technology focus on the electrolytes does not compete with Li-S and Li-O$_2$ batteries, which are focused on the electrode materials. Therefore, all-solid-state Li-S and Li-O$_2$ batteries are goals in the future as the batteries with both high energy density and high safety.

In recent years, from the standpoint of the battery package design, all-solid-state LIBs are considered to achieve higher volumetric energy density than conventional LIBs. Fig. 1-3 shows the schematics of the battery packages of the conventional liquid-type LIBs and all-solid-state LIBs [16]. In the battery packages, the conventional LIBs have to separate every single cell due to the existence of a liquid electrolyte and need extra space

8

between the single cells. In contrast, all-solid-state LIBs can allow the cell to stack in series as bipolar structures, which can significantly enhance the packaging efficiency of the battery. Therefore, all-solid-state LIBs will achieve higher energy density.

All-solid-state LIBs are roughly classified into two categories: thin-film batteries [17, 18] and bulk-type batteries [19, 20] as shown in Fig. 1-2 (b-1) and (b-2), respectively. In the 1990s, initial all-solid-state LIBs, which can be labeled as thin-film batteries, were reported by Bates et al. [21-23]. In these batteries, lithium phosphorus oxynitride (LiPON) glass, which has much lower conductivity (3.3×10^{-6} S/cm at room temperature) than conventional liquid electrolytes, was used as a solid electrolyte. Therefore, thin solid electrolyte layer, less than ~1 μm, was used to reduce the total resistance and battery performance was investigated. Amazingly, the thin-film-type of all-solid-state LIBs show dazzling cycle performance without any capacity loss over tens of thousands of cycles. It is considered that such a long cycle life is derived not only from the wide electrochemical window of LiPON but also from no side-reactions caused by the migration of counter anion. Therefore, these experiments have suggested that the all-solid-state LIBs can achieve longer cycle life than liquid-type LIBs. On the other hand, the bulk-type of solid-state LIBs, because of having higher energy density as compared to thin-film batteries, have attracted a growing interest (Fig. 1-2(b)). In order to increase the capacity of the bulk-type batteries, bulky electrodes were used. In this case, the electrodes have to include Li-ion-conducting ceramics (LICCs) and an active material; LICCs are mixed into the electrode layer to form Li-ion conductive pathways [24]. In bulk-type batteries, high ionic conductive electrolytes

9

are required. For this reason, numerous solid electrolytes have been suggested as discussed in *section 1.4.1*.
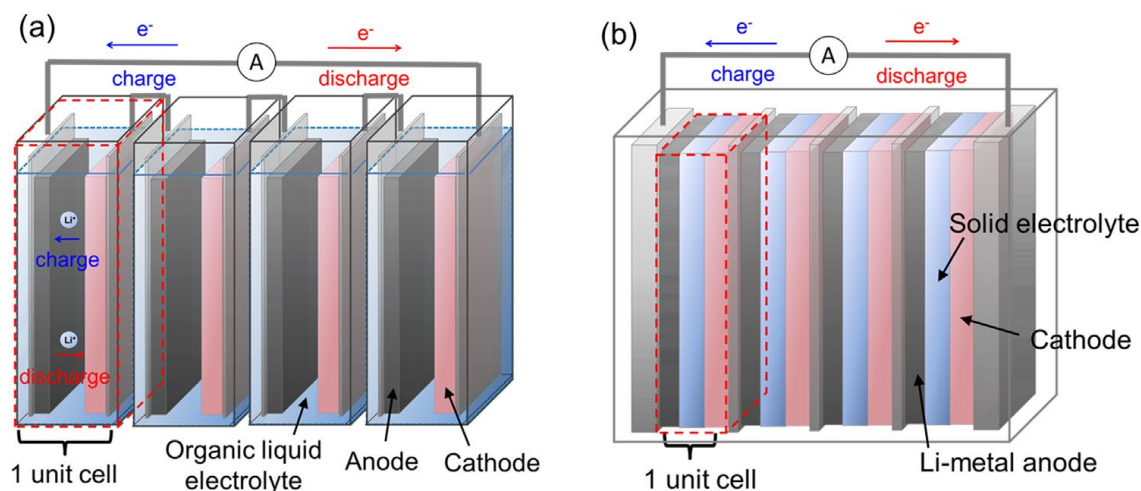
Fig. 1-3. Schematic of the battery packages of (a) conventional stacked liquid-type LIBs and (b) in-series stacked bipolar all-solid-state LIBs [16]

1.4 Solid electrolytes

Solid electrolytes can be classified into three types: inorganic electrolytes, polymer electrolytes, and polymer/inorganic composite electrolytes. The inorganic electrolytes are essential components in post LIBs as described above. On the other hand, polymer electrolytes have been also investigated owing to their flexibility which is difficult to obtain in inorganic solids. The polymer/inorganic composite electrolytes have been developed to establish a mutually complementary relationship. In this section, the detailed features of each type and more detailed introduction of the important materials in this dissertation are described.

1.4.1 Inorganic electrolytes

Inorganic electrolytes can be divided into three types in terms of the different heteroatoms in their ligands: nitride electrolytes, sulfide and oxide.   The conductivities of inorganic electrolytes are summarized in Table 1-1.

Table 1-1. Summary of properties of inorganic solid electrolytes

Composition	Ionic conductivity (S/cm) at R. T.	References
Nitride electrolytes		
Li_3N	1×10^{-3}	[25]
Sulfide electrolytes		
$80Li_2S\text{-}20P_2S_5$ (glass)	2×10^{-4}	[26]
$80Li_2S\text{-}20P_2S_5$ (glass-ceramic)	9×10^{-4}	[26]
$80Li_2S\text{-}20P_2S_5$ (glass-ceramic)	7.2×10^{-4}	[27]
$75Li_2S\text{-}25P_2S_5$ (ceramic)		[28]
$74.4Li_2S\text{-}2.4GeS_2\text{-}23.2P_2S_5$	1.2×10^{-3}	[29]
$70L_{i2}S\text{-}30P_2S_5$ (glass)	9.2×10^{-5}	[30]
$70Li_2S\text{-}30P_2S_5$ (glass-ceramic)	3.2×10^{-3}	[30]

Composition	Ionic conductivity (S/cm) at R. T.	References
Oxide electrolytes		
\<Garnet-type\>		
Tetragonal $Li_7La_3Zr_2O_{12}$	1.63×10^{-6} (bulk)	[31]
Tetragonal $Li_7La_3Zr_2O_{12}$	5.59×10^{-6} (grain boundary)	[32]
Tetragonal $Li_7La_3Zr_2O_{12}$	3.12×10^{-6}	
Cubic $Li_7La_3Zr_2O_{12}$	2.44×10^{-4}	[33]
Cubic $Li_7La_3Zr_2O_{12}$	1.39×10^{-4}	[34]
Cubic $Li_7La_3Zr_2O_{12}$	4×10^{-4}	[35]
$Li_7La_3Zr_2O_{12}$	$\sim10^{-4}$ (25 °C)	[36]
$Li_7La_3Zr_2O_{12}$	$\sim10^{-7}$ (25 °C)	[37]
Cubic $Li_{6.6}La_3Zr_{1.8}Mo_{0.2}O_{12}$	5.09×10^{-4}	[38]
Cubic $Li_7La_3Zr_2O_{12}$	3.2×10^{-4}	[39]
Cubic $Li_7La_3Zr_2O_{12}$	2×10^{-4} (30 °C)	[40]
Cubic-$Li_{6.55}La_3Zr_{1.55}Ta0.45O_{12}$	$\sim10^{-3}$	[41]
$Li_7La_3Zr_2O_{12}$	1.67×10^{-6}	[42]

Composition	Ionic conductivity (S/cm) at R. T.	References
<LLTO-type>		
$Li_{0.34}La_{0.51}TiO_{2.94}$	2×10^{-5}	[43]
$Li_5La_3Ta_2O_{12}$	1.3×10^{-4}	[44]
$Li_{0.45}La_{0.48}TaO_3$	8.75×10^{-4}	[45]
$Li_{3/8}Sr_{7/16}Ta_{3/4}Zr_{1/4}O_3$	2.7×10^{-4} (27 °C)	[46]
$Li_{3/8}Sr_{7/16}Ta_{3/4}Zr_{1/4}O_3$	2×10^{-4} (27 °C)	[47]
$Li_{3/8}Sr_{7/16}Ta_{3/4}Hf_{1/4}O_3$	3.8×10^{-4} (25 °C)	[48]
<NASICON-type>		
$Li_{1.3}Al_{0.3}Ti_{1.7}(PO_4)_3$ (ceramic)	7×10^{-4}	[49]
$Li_{1.4}Al_{0.4}Ti_{1.6}(PO_4)_3$ (glass-ceramic)	5.16×10^{-4}	[50]
$Li_{1.3}Al_{0.3}Ti_{1.7}(PO_4)_3$ (glass-ceramic)	7×10^{-4} (30 °C)	[51]
$Li_{1.5}Al_{0.5}Ge_{1.5}(PO_4)_3$ (glass-ceramic)	4.0×10^{-4} (27 °C)	[52]
Li_2O-Al_2O_3-SiO_2-P_2O_5-TiO_2-GeO_2	1×10^{-4}	[53]
Li_2O-Al_2O_3-SiO_2-P_2O_5-TiO_2	3×10^{-4}	

Singl-crystal Lithium nitride (Li_3N) is one of nitride electrolytes. Li_3N can show satisfactory ionic conductivities (~10^{-3} S/cm). However decomposition voltages were too low for high energy density [25]. In sulfide electrolytes, numerous materials based on

(100-x)Li_2S-xP_2S_5 have been discovered. Sulfide electrolytes, in a part of Table 1-1, show the reported conductivity of x=20, 25 and 30 in (100-x)Li_2S-xP_2S_5 depending on the phases. GeS_2 blended materials, such as Li_2S-GeS_2-P_2S_5, are one of the famous sulfide materials [29]. However sulfide electrolytes are suffering from hydrogen sulfide evolution caused by hygroscopic nature.

Oxide electrolytes are expected as the promising materials without toxic gas evolution. The following types of inorganic materials have been developed as oxide electrolytes with relatively high ionic conductivities: garnet-type (e.g., $Li_xLa_2M_3O_{12}$ (M = Zr, Ta, Nb)), Perovskite-type ($Li_{3x}La_{2/3-x}TiO_3$), NASICON-type (e.g., $Li_{1+x}Ti_{2-x}M_x(PO_4)_3$ (M = Al, Ga, In, Sc)).

Garnet-type materials [31-42] in oxide electrolytes can crystallize as two different phases [54,55]. It has been reported that the cubic structure (c-LLZO) has an ionic conductivity two or three orders of magnitude higher than that of the tetragonal structure (t-LLZO) (10^{-4} vs 10^{-7} S/cm) [56-58]. These garnet-type of Li-ion conductors confer the excellent electrochemical stability of ~6 V against Li metal and low electronic conductivity [59]. However, the handleability of garnet-type Li^+ conductors is limited by their reactivity with ambient air, such as H_2O or CO_2. Perovskite-type materials are Li-doped lanthanum titanate perovskite structure. Because La has larger radius and higher valence, the structure can possess more vacancies, leading Li-ion to move smoothly according to the defect-type mechanism to obtain high bulk conductivity (~10^{-3} S/cm) [60-62]. The resistance of the grain boundary of LLTO is extremely high. LLTO having grain boundary (polycrystalline)

has a total conductivity of 10^{-5} S/cm at room temperature, which is two orders of magnitude lower than the bulk conductivity. This is caused by chemical and structural deviations and impurity formation around the grain boundaries [63, 64].

In 1976, the sodium superionic conductor (NASICON) was reported by Goodenough et al. [65]. NASICON has the general formula $Na_{1+x}Zr_2P_{3-x}Si_xO_{12}$ obtained by the partial substitution of P with Si in $NaM_2(PO_4)_3$ (M = Ge, Ti, or Zr). NASICON for Li-ion conductors (NASICON-type) can be attained by replacing Na with Li. As shown in Fig. 1-4, crystalline NASICON-type possesses covalent $[M_2(PO_4)_3]^-$ frameworks, including corner-sharing PO_6 octahedral and MO_4 tetrahedral units. Due to the 3D connected framework, Li-ion conduction is possible in the interstitial sites [66]. However, this 3D connected framework leads a decrease in ionic conductivity owing to the following reasons: as the original channel is optimal for Na^+, it is too large for Li^+, whose ionic radius is smaller than Na^+, to migrate efficiency [67]. Lots of partially Al-substituted materials for Ti or Ge in NASICON-type, resulting in $Li_{1+x}Al_xTi_{2-x}(PO_4)_3$ (LATP) or $Li_{1+x}Al_xGe_{2-x}(PO_4)_3$ (LAGP), have been reported because trivalent Al has a smaller ionic radius than those of Ti or Ge [49-52]. NASICON-type materials have attracted considerable attention as promising LICCs because of the high bulk ion conductivity (~10^{-3} S/cm) and high stability against ambient air, especially moisture [68-72]. For these reasons, in this dissertation, NASICON-type materials are mainly used. Incidentally, an Al-substituted NASICON-type has been firstly developed and commercialized by Ohara Corporation.
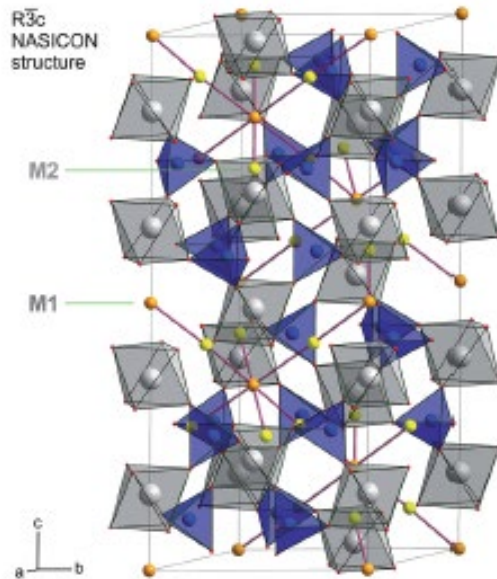
Fig. 1-4. Crystal structure of NASICON-type. Corner-sharing TiO_6 octahedra and PO_4 tetrahedral units are depiceted in gray and blue, respectively. The site occupancy is controlled by the amount of substituted Al^{3+} cations which replace the Ti^{4+} ions. Orange and yellow spheres represent possible Li sites the ions may use to diffuse through the crystal lattice [73].

Generally, in these materials, polycrystalline LICC powders are compacted or sintered to form LICC discs, which are then used as solid electrolyte layer in batteries [74, 75]. Although the intragrain impedance to Li transport is low, the high-impedance grain boundary and interparticle interfacial resistances increase the overall impedance of the disc. Therefore, these drawbacks make them too resistive to be used in all-solid-state batteries with target current densities similar to those of conventional LIBs [75]. Furthermore, LICC disc tends to be brittle and prone to cracking [4, 76, 77]. Therefore, the LICC disc for battery applications needs much greater than 100 μm. This increases the resistance and

16

makes them impractical in battery applications [77]. Therefore, approaches to making polymer/inorganic composite electrolytes, with ceramic particles embedded in a polymer electrolyte matrix, seem to improve their fracture toughness.

1.4.2 Polymer electrolytes

In addition to flexibility and safety, solid polymer electrolytes (SPEs) have the merit of easy manufacturing [78, 79]. Numerous SPEs, such as polyether, polyester, polyamine, polysulfide, etc., have been investigated [80-83]. Especially, a class of polyethyelene oxide (PEO)-based electrolytes is one of the famous polymer electrolytes owing to their property to solvate several Li salts with the interaction of its ether oxygens with cations [84]. However, PEO-based electrolytes usually have high degree of crystallization, leading to a low ionic conductivity at room temperature (10^{-6}–10^{-8} S/cm) [85]. This drawback is a serious problem not only for PEO but also for all SPEs. Therefore, their excellence in handling and processability for commercial applications are unfortunately off-set by the drawback and the practical usage on any application has been limited.

1.4.3 Polymer/inorganic composite electrolytes

Numerous studies have been explored on polymer/inorganic composite materials. Depending on the inorganic species as the additive, polymer/inorganic composite materials can be divided into two parts; passive additives and active additives. Passive additives, such as SiO_2, TiO_2, etc., are not involved in Li-ion conduction. However, they act as not only a

support matrix to improve mechanical characteristics but also restrict the recrystallization of polymer chains. It has been proposed that the addition of passive additives to SPEs can improve the mechanical properties [86], the conductivity and Li-ion transference number [87, 88]. Numerous types of the additives, such as different types, particle sizes and weight % content, have been searched [89, 90].

On the other hand, LICC materials have been also studied as active additives in the composite electrolytes. Active additives provide the same effects of the addition of passive additives, which can show the enhancement of mechanical toughness and the inhabitation of polymer recrystallization. Furthermore, polymer/inorganic composite electrolytes with active additives can enhance overall Li-ion conductivity. Huang et al. [91] and Zheng et al. [92] reported polymer/inorganic composite electrolyte with active additives. They provided insights in regard to Li-ion mobility in composite electrolytes as shown in Fig. 1-5 and Fig. 1-6 reprinted with references [91, 92]. In higher weight % content of active additives, Li-ion preferably moved through the ceramic phase instead of the polymer phase or polymer/ceramic interfaces. To further improve the conductivities of polymer/inorganic composite electrolytes with active additives, it is necessary to decrease the interfacial resistance between the polymer and ceramic which limits the enhancement of the entire conductivities.

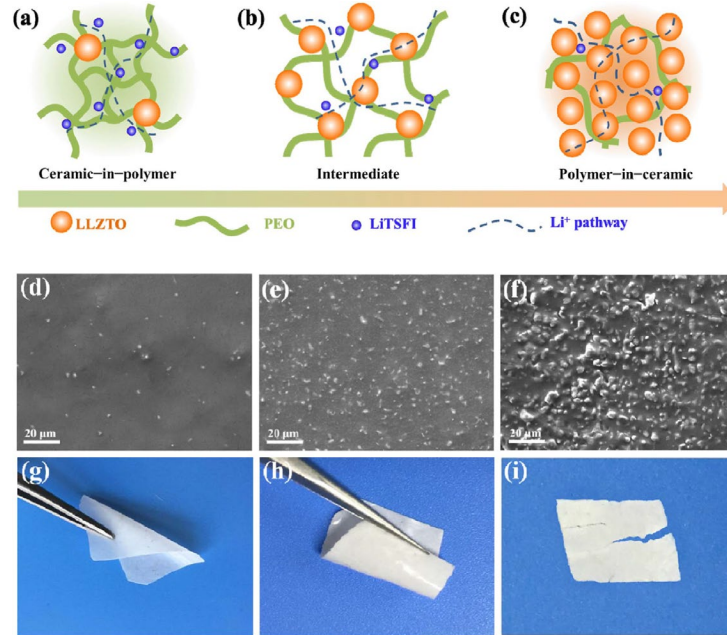Fig. 1-5. Schematic illustration for composite electrolytes with LLZO; (a) "ceramic-in-polymer", (b) "intermediate" and (c) "polymer-in-ceramic", depending on the concentration of inorganic electrolytes in composite electrolytes; (1-x) wt%[PEO$_8$-LiTFSI]- x wt% LLZTO; (d, g) 10, (e, h) 50 and (f, i) 80 wt% [91]
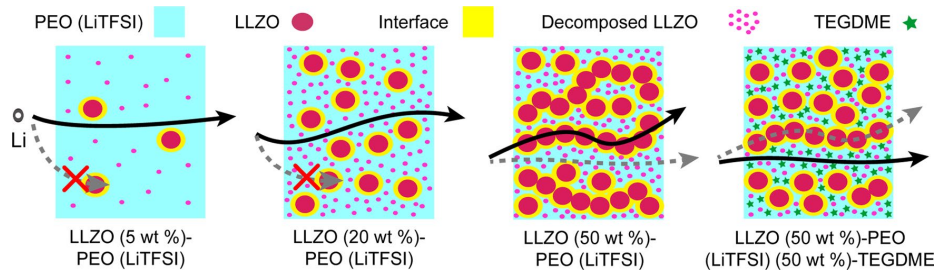

Fig. 1-6. Schematic diagram of Li-ion pathways in a PEO(LiTFSI)-LLZO composite electrolytes [92].

1.5   Key technical problems of solid electrolytes and target of this dissertation

As a LICC disc tends to be brittle and prone to cracking, they are not suitable for application to large sizes without increasing excessive thickness, which results in unacceptable weights and higher resistance. On the other hand, although SPEs can exhibit flexibility, safety and ease of manufacturing, their own conductivities limit their practical usage. The polymer/inorganic composite electrolytes have been developed to establish a mutually complementary relationship between features of SPEs and LICCs. However, the resistance enhanced issues, such as SPEs, the LICC–polymer, and the LICC–LICC contact interfaces, still persist.

Ideally, LICCs should be embedded as a single layer in the polymer matrix avoiding LICC-LICC contacts and polymer-LICC contacts. Here, in order to move towards this ideal and enhance the overall conductivities, this dissertation first focuses on details of the newly designed polymer/inorganic composite electrolytes, as well as processing techniques that will be applicable to a future-generation of all-solid-state batteries of high power density, high energy density, and superior safety.

In Chapter 2, novel polymer/inorganic composite layers are described and Li-ion conduction mechanisms are elucidated by AC impedance spectroscopic measurements. This work was previously published as "Fabrication and impedance analysis for designed composite layers with polymer and inorganic electrolytes leading to high conductivity" in *Solid State Ionics*. Chapter 3, which was published previously as the processing and impedance analysis in a part of "Flexible Ion-Conducting Composite Membranes for

Lithium Batteries in *Advanced Energy Materials* and Hybridizing mono-layered inorganic electrolytes and polymer leading to high conductivity and low activation energy for Li-ion batteries" (submitted to *Solid State Ionics*), describes the fabrication of the newly designed one-particle-thick membranes, an effort toward higher conductivities compared to the commercial solid-state electrolytes. The thinner one-particle-thick membranes, which provide high energy/power density and low overpotential in batteries, are shown in Chapter 4. This was submitted to *Solid State Ionics*. The end of Chapter 4 indicates that these membranes resist the penetration of lithium dendrites, as a part of "Flexible Ion-Conducting Composite Membranes for Lithium Batteries in *Advanced Energy Materials*."

1.6　References

[1] Whittingham M.S., Progress in Solid State Chemistry 12 (1978) 41-99

[2] Mizushima K., Jones P.C., Wiseman P., Goodenough J.B., 3-4 (1981) 171-174

[3] Tarascon J.-M., Armand M., Nature 414 (2001) 359-367.

[4] Goodenough J.B., Park K.-S., J. Am. Chem. Soc. 135 (2013) 1167-1176.

[5] Armand M. & Tarascon J.-M., Nature 451 (2008) 652-657.

[6] Kato Y., Hori S., Saito T., Suzuki K., Hirayama M., Mitsui A., Yonemura M., Iba H., Kanno R. Nature Energy 1 (2016) 1-7.

[7] Fang R., Zhao S., Sun Z, Wang D,-W, Cheng H. –M., Advanced Materials, 29 (2017) 48.

[8] Manthiram, A., Chung S.-H., C. Zu, 27 (2015) 1980-2006.

[9] Borchardt, L., M. Oschatz, S. Kaskel, Chemistry – A European Journal, 22 (2016) 7324-7351.

[10] Amine, K., Belharouak I., Chen Z., Tran T., Yumoto H., Ota N., Myung S. –T., Sun Y. –K., Advanced Materials, **22** (2010) 3052-3057.

[11] Rahman, M.A., Wang X., Wen C., Journal of the Electrochemical Society, 160 (2013) A1759-A1771.

[12] Iwamoto K., Aotani N., Takada K., Kondo S. Solid State Ionics 79 (1995) 288-291.

[13] Bates J.B., Dudney N.J., Neudecker B., Ueda A., Evans C.D. Solid State Ionics 135 (2000) 33-45.

[14] Jones S.D., Akridge J.R., Shokoohi F.K. Solid State Ionics 69 (1994) 357-368.

[15] Ogawa M., Yoshida K., Harada K. SEI Technical review 74 (2012) 88-90.

[16] Gambe Y., Sun Y., Honma I. Scientific Reports 5 (2015) 8869.

[17] Kanehori K., Matsumoto K., Miyauchi K., Kudo T. Solid State Ionics 14451448 (1983) 9-10.

[18] Bates J.B, Dudney N.J., Neudecker B., Ueda A.,Evans C.D., Solid State Ionics 135 (2000) 3345.

[19] Malugani J., Fahys B., Mercier R., Robert G., Duchange J., Baudry S., Broussely M., Gabano J. Solid State Ionics, 659665 (1983) 9-10.

[20] Sakuda A., Kitaura H., Hayashi A., Tatsumisago M., Hosoda Y., Nagakane T., Sakamoto A. Chem. Lett. 41 (2012) 260261.

[21] Bates J.B., Dudney N.J., Gruzalski G.R., Zuhr R.A., Choudhury A., Luck C.F. J. Power Sources 103 (1993) 43-44.

[22] Bates J.B. Electron. Eng. 69 (1997) 63.

[23] Neudecker B.J., Dudney N.J. & Bates J.B., J. Electrochem. Soc. 147 (2000) 517.

[24] Sakuda A, J.Ceramic Society of Japan, 126 (9) 675-683 (2018)

[25] Boukamp B., Huggins R., Phys. Lett. A 58 (1976) 231-233.

[26] Hayashi A., Hama S., Morimoto H., Tatsumisago M, Minami T., Chem. Lett. 30 (2001) 872-873.

[27] Hayashi A., Hama S., Minami T., Tatsumisago M. Electrochem. Commun. 5 (2003) 111-114.

[28] Liu Z, Fu W, Payzant A, Yu X, Wu Z, Dudney N. J, Kiggans J, Hong k, Rondinone A. J, Liang C, J. Am. Chem. Soc. 135 (2013) 975-978

[29] Trevey J.E., Jung Y.S., Lee S.-H., Electrochim. Acta 56 (2011) 4243-4247

[30] Tatsumisago M., Mizuno F. & Hayashi A., J. Power Sources 159 (2006) 193-199.

[31] Awaka J., Kijima N., Hayakawa H. & Akimoto J., J. Solid State Chem. 182 (2009) 2046-2052.

[32] Kokal I., Somer M., Notten P.H.L. & Hintzen H.T., Solid State Ionics, 185 (2011) 42-46.

[33] Murugan R., Thangadurai V., Weppner W., Angew. Chem. Int. Ed. 46 (2007) 7778-7781.

[34] Shimonishi Y., Toda A., Zhang T., Atsushi Hirano A., Imanishi N., Yamamoto O., Takeda Y., Solid State Ionics 183 (2011) 48-53.

[35] Sakamoto J., Rangasamy E., Kim H., Kim Y., Wolfenstine J. Nanotechnology 24 (2013) 424005.

[36] Rosenkiewitz N., Schuhmacher J., Bockmeyer M, Deubener J., J. Power Sources 278 (2015) 104-108.

[37] Tan J.J., Ashutosh T.A., Electrochem. Solid-State Lett. 15(3) (2012) A37-A39.

[38] Liu X., Li Y., Yang T., Cao Z., He W., Gao Y., Liu J., Li G., Li Z., J. Amer. Ceram. Soc. 100 (2017) 1527-1533.

[39] Kim K.-W., Yang S.-H., Kim M.Y., Lee M.S., Lim J., Chang D.R., Kim H.-S. J. Ind. Eng. Chem. 36 (2016) 279-283.

[40] Shao C., Liu H., Yu Z., Zheng Z., Sun N. & Diao C., Solid State Ionics 287 (2016) 13-16.

[41] Inada R., Yasuda S., Hosokawa H., Saito M., Tojo T., Sakurai Y., Batteries 4 (2018) 26; doi:10.3390/batteries4020026

[42] Chen R.J., Huang M., Huang W.Z., Yang Shen Y., Lin Y.H., Nan C.-W., J. Mater. Chem. A 2 (2014) 13277-13282.

[43] Inaguma Y., Liquan C., Itoh M., Nakamura T., Uchida T., Ikuta H., Wakihara M. Solid State Commun. 86 (10) (1993) 689-693.

[44] Kotobuki M., Kanamura K., Ceram. Int. 39 (2013) 6481-6487.

[45] Furusawa S.-I., Tabuchi H., Sugiyama T., Tao S. W., Irvine J.T.S., Solid State Ionics 176 (2005) 553-558.

[46] Inada R., Kimura K., Kusakabe K., Tojo T., Sakurai Y. Solid State Ionics 261 (2014) 95-99.

[47] Kimura K., Wagatsuma K., Tojo T., Inada R., Sakurai Y. Ceram. Int. 42 (2016) 5546-5552.

[48] Huang B., Xu B., Li Y., Zhou W., You Y., Zhong S., Wang C.A., Goodenough J.B. ACS Appl. Mater. Interfaces 8 (2016) 14552-14557.

[49] Aono H., Sugimoto E., Sadaoka Y., Imanaka N., Adachi G.Y., J. Electrochem. Soc. 136 (2) (1989) 590-591.

[50] Xu X.X., Wen Z.Y., Yang X.L., Zhang J.C., Gu Z.H., Solid State Ionics 177 (2006) 2611-2615.

[51] Aono H., Imanaka N., Adachi G.-y. Acc. Chem. Res. 27 (1994) 265-270.

[52] Fu J. Solid State Ionics 104 (1997) 191-194.

[53] Nakajima K., Katoh T., Inda Y., Hoffman B., Lithium ion conductive glass ceramics Lithium Ion (2010).:Properties and application in lithium metal batteries. Symposium on Energy Storage beyond

[54] Awaka J., Kijima N., Hayakawa H. & Akimoto J.J. Solid State Chem. 182 (2009) 2046e2052.

[55] Geiger C.A., Alekseev E., Lazic B., Fisch M., Armbruster T., Langner R., Fechtelkord M., Kim N., Pettke T. & Weppner W. Inorg. Chem. 50 (2011) 1089-1097.

[56] Yeandel S., Chapman B.J., Slater P.R., Goddard P. J. Phys. Chem. C, 122 (2018) 27811-27819

[57] Thompson T., Wolfenstine J., Allen J.L., Johannes M., Huq A., David I.N., Sakamoto J. J. Mater. Chem. A 2 (2014) 13431.

[58] Awaka J., Kijima N., Hayakawa H., Akimoto J. Journal of Solid State Chemistry 182 (2009) 2046-2052.

[59] Thangadurai V., Pinzaru D., Narayanan S., Baral A.K. J. Phys. Chem. Lett. 6 (2015) 292-299.

[60] Thangadurai V., Weppner W. Ionics, 12 (2006) 81-92.

[61] Knauth P. Solid State Ionics, 180 (2009) 911-916.

[62] Stramare S., Thangadurai V., Weppner W. Chem. Mater. 15 (2003) 3974.

[63] Aguesse F., Lopez del Amo J., Roddatis V., Aguadero A., Kilner J.A. Adv. Mater. Interface 7 (2014) 1300143.

[64] Ma C., Chen K., Liang C., Nan C., Ishikawa R., More K., Chi M. Energy. Environ. Sci. 7 (2014) 1638-1642.

[65] Goodenough J., Hong H.P., Kafalas J. Mater. Res. Bull. 11 (1976) 203-220.

[66] Thanadurai V., Weppner W. Ionics 8 (2002) 281.

[67] Hong H.P. Mater. Res. Bull. 13 (1978) 117-124.

24

[68] Aono H., Imanaka N. & Adachi G.-Y. Acc. Chem. Res. 27 (1994) 265-270.

[69] Adachi G.-Y., Imanaka N. & Aono H. Adv. Mater. 8 (1996) 127-135.

[70] Thangadurai V., Shukla A.K. & Gopalakrishnan J. J. Mater. Chem. 9 (1999) 739-741.

[71] Sugantha M. & Varadaraju U.V. Solid State Ionics 95 (1997) 201-205.

[72] Leo C.J., Subbarao G.V. & Chowdari B.V.R. J. Mater. Chem. 12 (2002) 1848-1853.

[73] Breuer S., Prutsch D., Ma Q., Epp V., Preishuber-Pflügl F., Tietz F., Wilkening M., J. Mater. Chem. A 3 (2015) 21343-21350

[74] J. Sakamoto , E. Rangasamy , H. Kim , Y. Kim , J. Wolfenstine , Nanotechnology 24 (2013), 424005 .

[75] W. E. Tenhaeff, Rangasamy E., Y. Wang, A. P. Sokolov, J. Wolfenstine, J. Sakamoto, N. J. Dudney, Chem ElectroChem 2014, 1, 375

[76] Lithium Air Batteries: Fundamentals (Eds: N. Imanishi, A. C. Luntz, P. Bruce), Springer, New York 2014

[77] H. Lee, M. Yanilmaz, O. Toprakci, K. Fu, X. Zhang, Energy Environ. Sci. 7 (2014), 3857–3886.

[78] Prasanth R., Aravindan V. & Srinivasan M., J. Power Sources 202 (2012) 299-307.

[79] Ramesh S. & Ng H., Solid State Ionics 192 (2011) 2-5.

[80] P. V. Wright, Br. Polymer. J., 7, 319 (1975)

[81] Watanabe M, Rikukawa K, Sanui K, Ogata N, macromolecules, 17, 2908 (1984)

[82] Chiang C. K, Davis G.T, Harding A, Takahashi T, macromolecules, 18. 825 (1985)

[83] Clancy S, Shriver D.F, Ochymowycz A, Macromolecules, 19, 606 (1986)

[84] Scrosati B. Applications of electroactive polymers, Springer (1993) 182-222.

[85] Kim J.G., Son B., Mukherjee S., Schuppert N., Bates A., Kwon O., Choi M.J., Chung H.Y., Park S., J. Power Sources 282 (2015) 299-322.

[86] Weston J.E., Steele B.C.H., Solid State Ionics 7 (1982) 81-88.

[87] Croce F., Appetecchi G.B., Persi L., Scrosati B., Nature 394 (1998) 456-458.

[88] Croce F., Persi L., Scrosati B., Serraino-Fiory F., Plichta E., Hendrickson M.A. Electrochim. Acta 46 (2001) 2457-2461.

[89] Wang C.X., Xia Y.Y., Koumoto K., Sakai T., J., Electrochem. Soc. 149 (2002) A967-A972.

[90] Quartarone E., Mustarelli P. Chem. Soc. Rev. 40 (2011) 2525-2540.

[91] Huang J., Peng J., Ling S., Yang Q., Qiu J., Lu J., Zheng J., Li H., Chen

L.N. Chin. Phys. B 6 (2017) 068201.

[92] Zheng. J, H. Hu. Y. ACS Appl. Mater. Interfaces 10 (2018) 4113-4120

2 Fabrication and impedance analysis for designed composite layers with polymer and inorganic electrolytes

2.1 Introduction

Numerous studies have been published with respect to multi-particle thick inorganic/polymer composites in order to improve the mechanical strength of the LICC disc. However, this can reduce the Li-ion's mobility owing to high resistance from SPEs, the inorganic–polymer, and the inorganic–inorganic contact interfaces [1–5].

In this chapter, the newly designed composite layers (CLs) were suggested; CLs comprise a SPE and Li-ion-conducting ceramic particle (LICP) as a matrix, with particles arranged in a single layer towards the matrix. However, SPEs generally have low ionic conductivities at room temperature. Therefore, in order to reduce the total resistance, it is necessary to make the SPE thinner between the LICP and the electrodes. This is the most important point of this concept. In addition, it is anticipated that using flexible SPEs will help increase contact with the electrodes. Moreover, several other merits are expected. In this method, the CLs can be directly fabricated on the electrodes. Therefore, the CLs can be made as thin as possible without the additional supporting layer to obtain sufficient mechanical strength. Regarding the resistance components of CLs themselves, interfacial resistance should be considered to achieve a lower total resistance except for the bulk resistance of SPEs as mentioned above. Although CLs have no LICP–LICP contact, there

are LICP–polymer contacts in CLs. Abe et al. [1] suggested that the composite electrolytes using SPEs and ceramic electrolytes show high interfacial resistance and their contact area should be as small as possible to attain high Li-ion conductivities. In comparison with multi-particle thick LICP–polymer composites, CLs can minimize the LICP-polymer interfacial resistance. In this chapter, the fabrication of CLs is demonstrated; then, we study the impedance behaviors in order to understand the Li-ion transfer mechanism of CLs.

2.2 Experiments

2.2.1 Designed Composite layers

$Li_{1.3}Al_{0.3}Ti_{1.7}P_3O_{12}$ (LATP) was chosen from the viewpoints of its high Li-ion conductivity and stability in ambient air. The LATP particles (Toshima Manufacturing) were sieved from 45 μm to 53 μm-sized particles. By way of comparison, 50 μm-sized ZrO_2-based particles (Niimi NZ beads 50, Niimi Sangyo), which are insulators, were used.

2.2.2 Fabrication for Composite layers

A schematic of the process used to prepare the CLs is shown in Fig. 2-1 (a). The CLs were fabricated in a dry room (temperature: 21 °C, dew point: -65 °C). Polymer electrolyte, which consists of PEO with an electrolyte salt, Li bis(trifluoromethane sulfonyl) imide (PEO-LiTFSI), is well known as an adhesive for inorganic particles [6]. PEO (average Mw: 60,000, Aldrich) and LiTFSI (Panax) with [Li]/[O]=18 (i.e., the ratio of the ethylene oxide

unit [O] to Li [Li]) were chosen. Anhydrous acetonitrile (AN) containing 0.07 g of PEO-LiTFSI at 8 wt% was dropped on a stainless steel disk (SUS), which was employed as an electrode, and then dried at 80 °C for 30 min in order to remove AN. The thickness of the PEO-LiTFSI layer on the SUS was approximately 10 μm (SUS/PEO-LiTFSI). Next, sieved particles were dispersed to be arranged in a single layer on the PEO-LiTFSI with the SUS (SUS/PEO-LiTFSI/particles). The arranged ZrO_2-based or LATP particles in the single layer are visible in Fig. 2-1 (b) and Fig. 2-1(c). Moreover, SUS/PEO-LiTFSI was stacked on SUS/PEO-LiTFSI/particles to obtain the sandwich structure SUS/PEO-LiTFSI/particles/ PEO-LiTFSI/SUS, which was encapsulated in a 2032 coin cell with two springs that exert a small pressure on the sample. Finally, samples were placed in an oven at 80 °C, which is over the melting point of PEO (60 °C), for each retention period to embed the particles in the PEO-LiTFSI matrix. The abovementioned conditions for storing the CLs are crucial for the following reasons. First, defoaming of the microbubbles between the particles and the movement of PEO-LiTFSI around the particles enhances adhesion of the particles to the interface. Second, the thickness of PEO-LiTFSI (t-PEO-LiTFSI), which is slightly remained between the SUS electrode and the LATP particles, is decreased. The residual t-PEO-LiTFSI, which may possibly decrease total Li-ion conductivity, was hardly observed as shown in the cross-section SEM image in Fig. 2-2.

We obtained the ionic conductivities of CLs from AC impedance measurements of the SUS/CLs/SUS sandwich structure at room temperature (21 °C) in a dry room, as Imanishi et. al. reported using an Al/LATP disc/Al structure [7]. For the SUS/CLs/SUS with

29

LATP particles (CL-LATP) and the SUS/CLs/SUS with ZrO$_2$-based particles (CL-ZrO$_2$), we collected AC impedance measurements using a potentiostat (VMP3, Bio-Logic) in a frequency range from 1 Hz to 1 MHz (with a perturbation voltage of 10 mV) at room temperature for various retention periods. Impedance measurements for Arrhenius plots were performed at temperatures between -20 °C and 80 °C, controlled by a thermostatic oven (ESPEC).
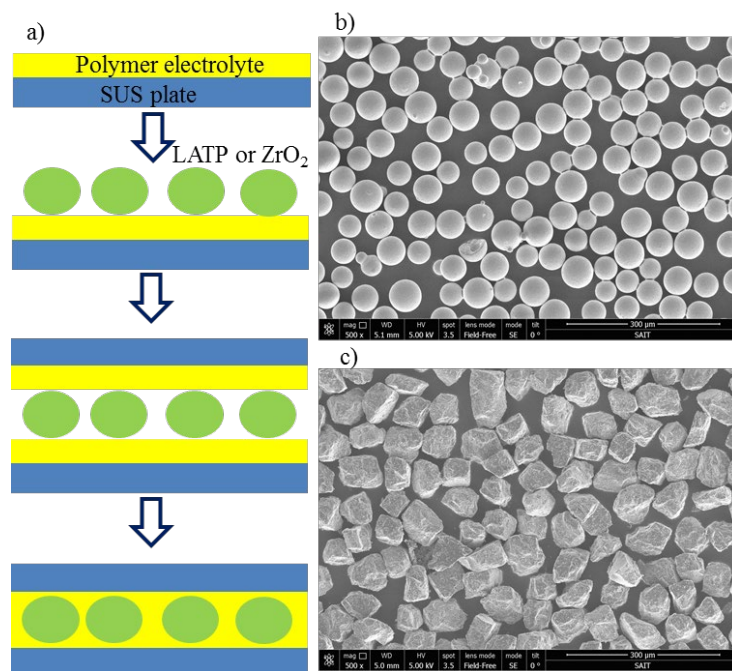

Fig. 2-1. (a) Schematic of the steps involved in the fabrication of CLs. Plane-view SEM images of arranged particles in a single layer on PEO-LiTFSI in the second step of the schematic: (b) ZrO$_2$-based particles and (c) LATP particles.
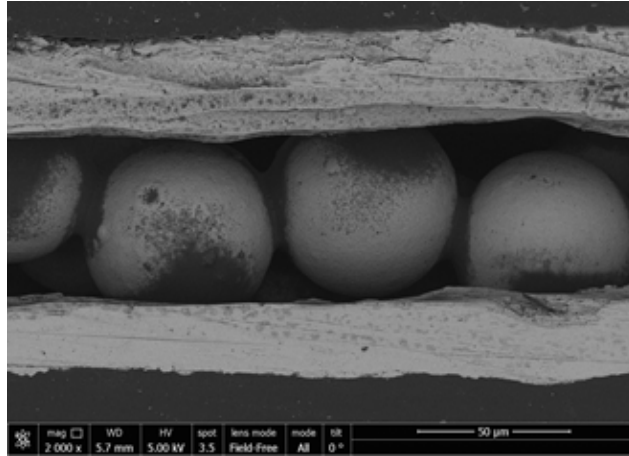
Fig. 2-2. Cross-section SEM image of the final CL-ZrO$_2$, prepared by using Cu foils instead of SUS plates for observing the state of t-PEO-LiTFSI. For the sampling the cross-section, Cu foils were used instead of the SUS plate.

2.3   Results and Discussion

To clarify the Li-ion transfer mechanism of CL-LATP, impedance behaviors were investigated in detail while comparing with the CL-ZrO$_2$. First of all, the impedance change of CL-ZrO$_2$ during 80 °C retention period was investigated. In Fig. 2-3(a), typical Nyquist plots are displayed at various 80 °C retention periods for the CL-ZrO$_2$. We observed one semicircle, which can be satisfactorily ascribed to a bulk resistance of the PEO-LiTFSI electrolyte, with a characteristic frequency of 100 kHz and the near-vertical line associated with electrode polarization. After the retention period of 21 days, the resistance of CL-ZrO$_2$ was 896 Ω. The thickness of CLs after the retention period of 21 days was 57 μm. The conductivity of CLs-ZrO$_2$ was around 0.0033 mS/cm at room temperature, which is almost the same as in previous reports [8]. Fig. 2-3(b) shows the Nyquist plot for CL-LATP at

31

various 80 °C retention periods. During the retention period of 3 hours for CL-LATP, the Nyquist plots showed a clear semicircle ascribed to the bulk resistance of PEO-LiTFSI, while others revealed small or no semicircles in the frequency range of 100 Hz to 1 MHz. Interestingly, the resistance drastically decreased during the 80 °C retention periods. After the retention period of 21 days, the resistance and thickness of CL-LATP were 21 Ω and 56 µm, respectively, corresponding to 0.14 mS/cm. This result demonstrates that the CLs prepared on the basis of our new concept show high Li-ion conductivity and can be directly prepared on the electrodes without any etching and sintering processes. These results indicate that the drastic decrease of the resistance during retention periods for CL-LATP is derived from the use of LICPs. These experiments were repeated thrice (CL-LATP #1, CL-LATP #2 and CL-LATP #3), as depicted in Fig. 2-4, to confirm the reproducibility of the results. The resistances of these three samples corresponded to 21 Ω (CL-LATP #1), 28 Ω (CL-LATP #2), and 16 Ω (CL-LATP #3).

Then, the frequency dependence of the impedance changes was investigated. Conductivity spectra, i.e., the real part of the complex conductivity (σ) plotted vs. frequency (log F), are shown for the CLs in Fig. 2-5. Electrode polarizations, which were shown as near-vertical line in lower frequency, were caused by fast Li-ion transport, causing a pile up of ions in front of the surface of the ion blocking electrode. Fig. 2-5 (a) shows the collections of conductivity spectra for CL-ZrO$_2$. From 100 Hz to 40 kHz, we observed near-flat area (DC plateaus), characterized by σ_p, for various retention periods. These plateaus are derived from Li-ion conduction within PEO-LiTFSI. As the result, σ_p

32

kept around 0.003 mS/cm at any retention periods. In Fig. 2-5 (b), conductivity spectra are

shown for CL-LATP. The frequency range of the DC plateaus, characterized by σ_q, changed

from 100 Hz to 40 kHz (the retention period of 3 hours) to 40 kHz to 1 MHz (the retention

period of 21 days). In addition, σ_q was shifted from 0.005 mS/cm to 0.14 mS/cm.
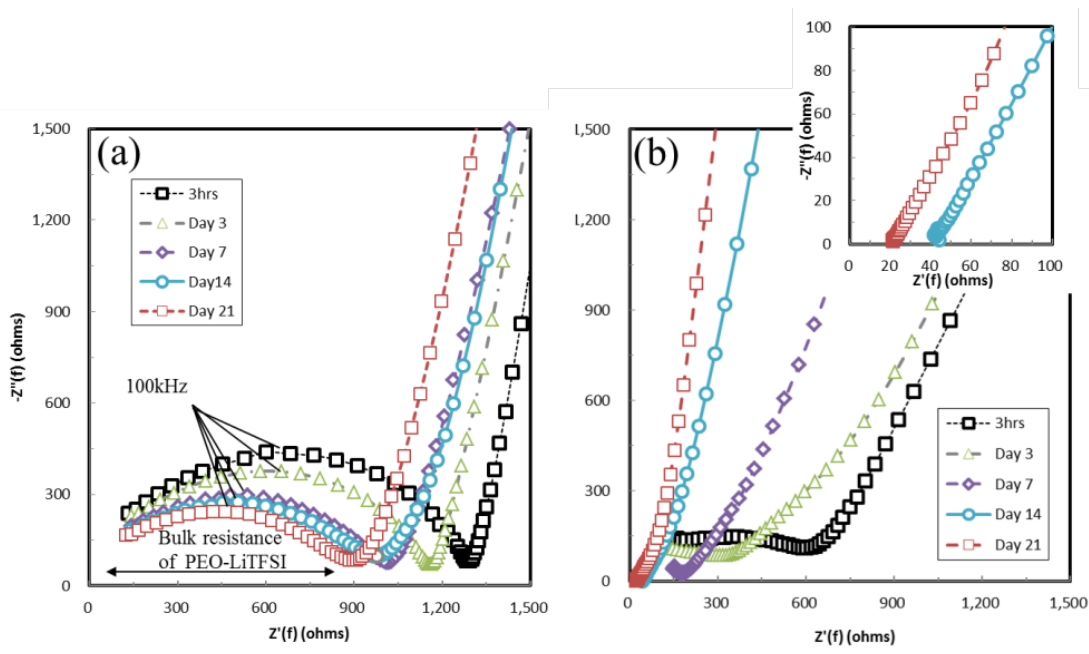
Fig. 2-3. Nyquist plots of the impedance data: (a) CL-ZrO$_2$ and (b)
CL-LATP. CL-ZrO$_2$ consists of PEO-LiTFSI and ZrO$_2$-based insulator
particles (Niimi Corp., 50 μm). CL-LATP consists of PEO-LiTFSI and
sieved LATP (Toshima, 45–53 μm).
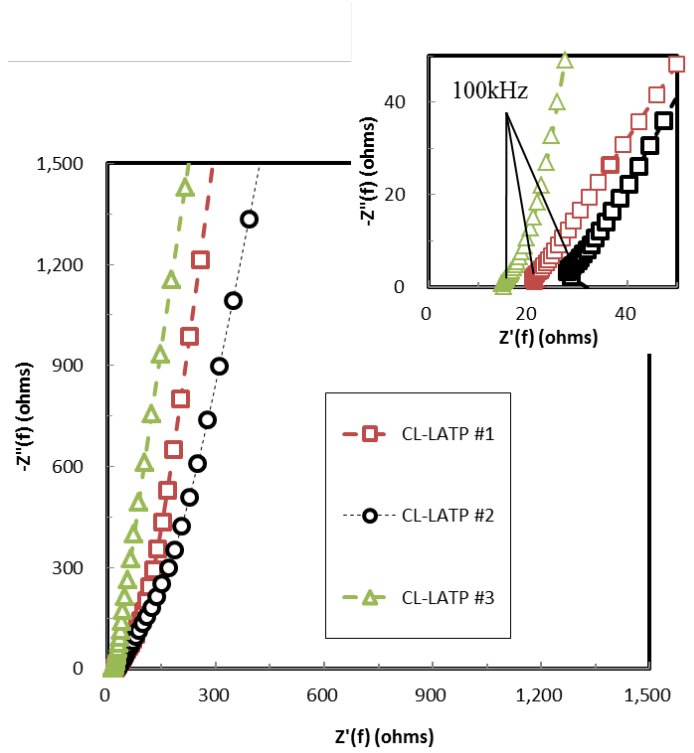
Fig. 2-4. Nyquist plots of the impedance data for three CL-LATP samples (CL-LATP #1, CL-LATP #2 and CL-LATP #3) after a retention period of 21 days. CL-LATP #1   is the main candidate for analysis in this research.

34
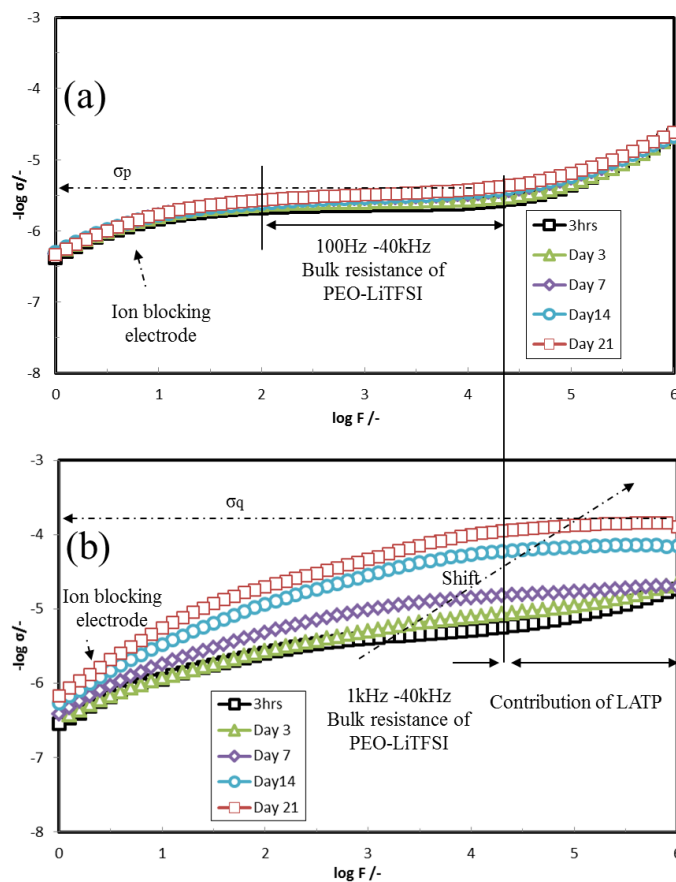
Fig. 2-5. Conductivity isotherms for various retention periods: (a) CL-ZrO$_2$ and (b) CL-LATP.

CLs offer two possible Li-ion conduction paths (Path A and Path B) as shown in Fig. 2-6. In the case of CL-ZrO$_2$, Li-ion has to move into Path A (PEO-LiTFSI) because Li-ion cannot move into Path B owing to the usage of ZrO$_2$-based insulator particles. Therefore, these plateaus for CL-ZrO$_2$ are derived from Li-ion conduction within PEO-LiTFSI. In addition, the DC 1 kHz-40 kHz plateau for CL-LATP, which is the state before shifting, is

35

almost the same as the case of CL-ZrO$_2$ (100 Hz-40 kHz). It indicates that the Li-ion conduction path of CL-LATP at the beginning stage of retention period is mainly Path A. On the other hand, it is estimated that the DC 40 kHz-1 MHz plateau after shifting is not associated with Path A but rather Path B. If Path A is still main conduction path, the conductivity of CL-LATP after 21 days should be the same as the CL-ZrO$_2$ because the whole thickness of CL-LATP after 21 days was the same as that of CL-ZrO$_2$. Hence, the frequency and conductivity shifts of the DC plateau for CL-LATP are derived from the shifting the Li-ion conduction path from Path A to Path B. This can be confirmed by the activation energy calculated from the Arrhenius plots as we will describe below. Here, the LATP resistance comprises the following resistances:

(i) interfacial resistance due to Li-ion transfer at the interface between t-PEO-LiTFSI and LATP particles,

(ii) bulk resistance of the polycrystalline LATP particles, and

(iii) grain boundary resistance of the polycrystalline LATP particles.

Among these factors, factor (ii) causes the semicircle over 1 MHz in the Nyquist plot [9, 10], which is out of the range in this measurement at room temperature. Therefore, the contribution of LATP in the range of 40 kHz to 1 MHz consists of factors (i) and (iii). With respect to the case of using LATP plates and PEO electrolytes, some reports indicated that one semicircle includes the resistance components of factors (i) and (iii) in the Nyquist plot [18, 11]. It is difficult to distinguish between factors (i) and (iii) when using the Nyquist

36

plot.
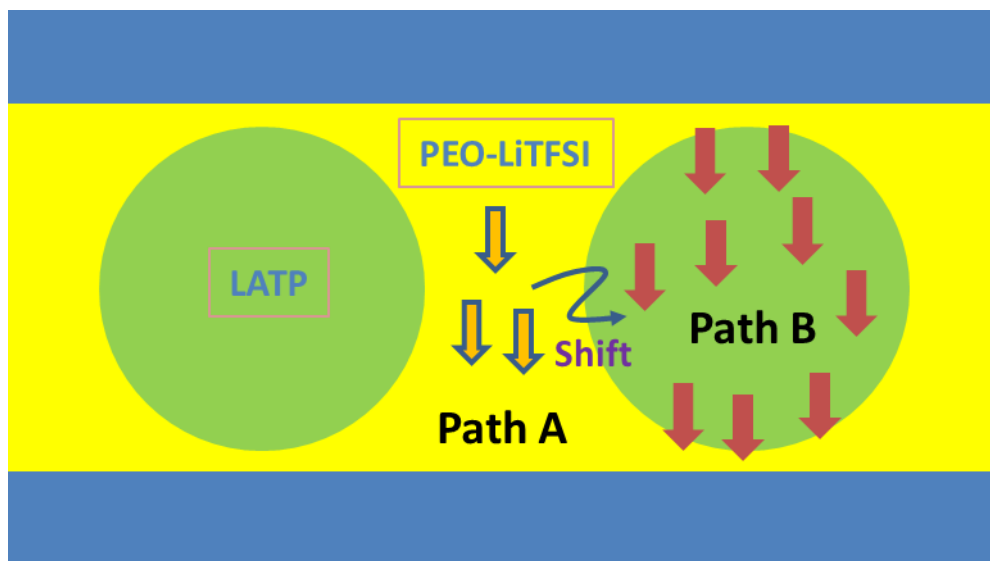
Fig. 2-6. Possible Li-ion conduction paths for CLs

Fig. 2-7 shows the temperature dependencies of ionic conductivity for CL-ZrO$_2$ and CL-LATP with a retention period of 21 days. Owing to local relaxation and segmental motion of the PEO chains above 55 °C, the Li-ion conductivity of CL-ZrO$_2$ increased to 0.24 mS/cm at 60 °C and 0.48 mS/cm at 80 °C. These are well matched to the findings of Shin et al. [8] and Chen et al. [12]. The plot was well fit by the Arrhenius equation, and the coefficients of determination (R^2) in all plots from -20 °C to 50 °C were greater than 0.98. We calculated the activation energy for Li-ion conduction in CL-ZrO$_2$ in the temperature range of -20 °C to 50 °C to be 123 kJ/mol, which also matches the results of Chen et al. [12]. We evaluated the activation energy for CL-LATP based on the slopes shown in Fig.

2-7, and arrived at an answer of 71 kJ/mol in the range of -20 °C to 50 °C. Comparing the calculated activation energy with those recently presented in the literature [7, 12, 13], this value is smaller than the activation energy of 122 kJ/mol in the range of -20 °C to 50 °C for PEO electrolytes, and larger than 0.44 eV (42.5 kJ/mol), which is the activation energy for the grain boundary resistance of LATP particles, as reported by Arbi et al. [13]. The activation energy of 71 kJ/mol cannot be identified as a specific factor because distinguishing some factors was difficult in the Nyquist plots. At least, however, the difference of activation energies between CL-LATP and CL-ZrO_2 indicates that the conduction path of CL-LATP is different from that of CL-ZrO_2 as mentioned in the discussion of Fig 2-5.
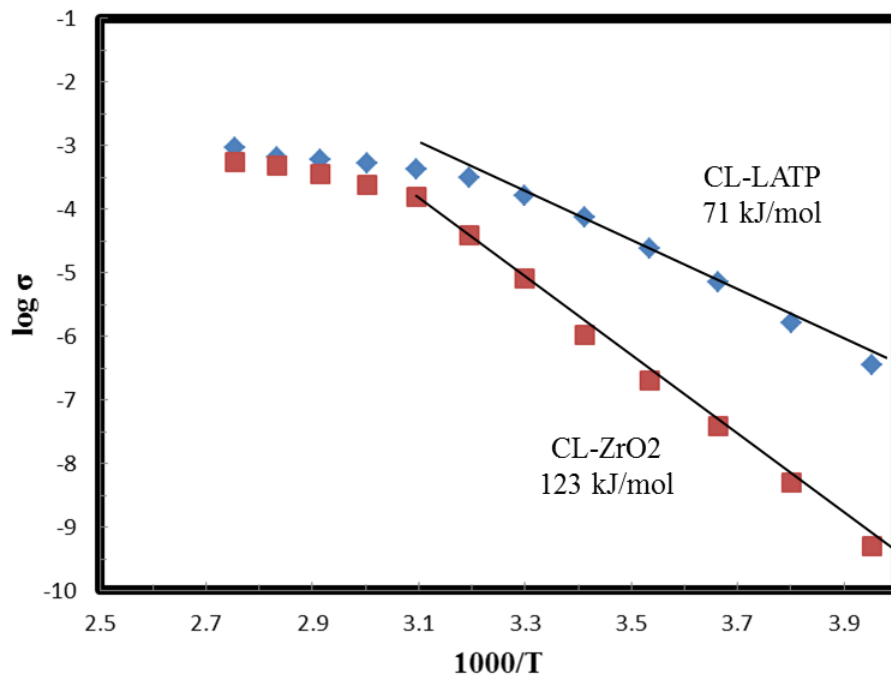
Fig. 2-7. Arrhenius plots for CL-LATP and CL-ZrO$_2$.

Finally, we performed additional experiments using different volume ratios of LATP particles/total particles to confirm the aforementioned phenomenon. LATP and ZrO_2-based particles were blended with selected LATP ratios of 34.0 vol% and 4.2 vol% (represented as CL-LATP(x): (CL-LATP(34.0) and CL-LATP(4.2), respectively). Fig. 2-8 shows that a higher value of x corresponds to a decrease in the resistance and an increase in the conductivity.

Fig. 2-8. (a) Nyquist plots for the impedance data of CL-LATP(x) after a retention period of 21 days: CL-LATP(0)(CL-ZrO₂), CL-LATP(4.2), CL-LATP(34.0) and CL-LATP(100)(CL-LATP). (b) Dependence of conductivities on volume ratios of LATP particles(x). These conductivities were calculated by using the values indicated by arrows at Nyquist plots in (a).

2.4 Conclusion

This chapter presented newly designed CLs, which are applicable to large-scale production. In addition, we investigated the Li-ion transfer mechanism by using AC i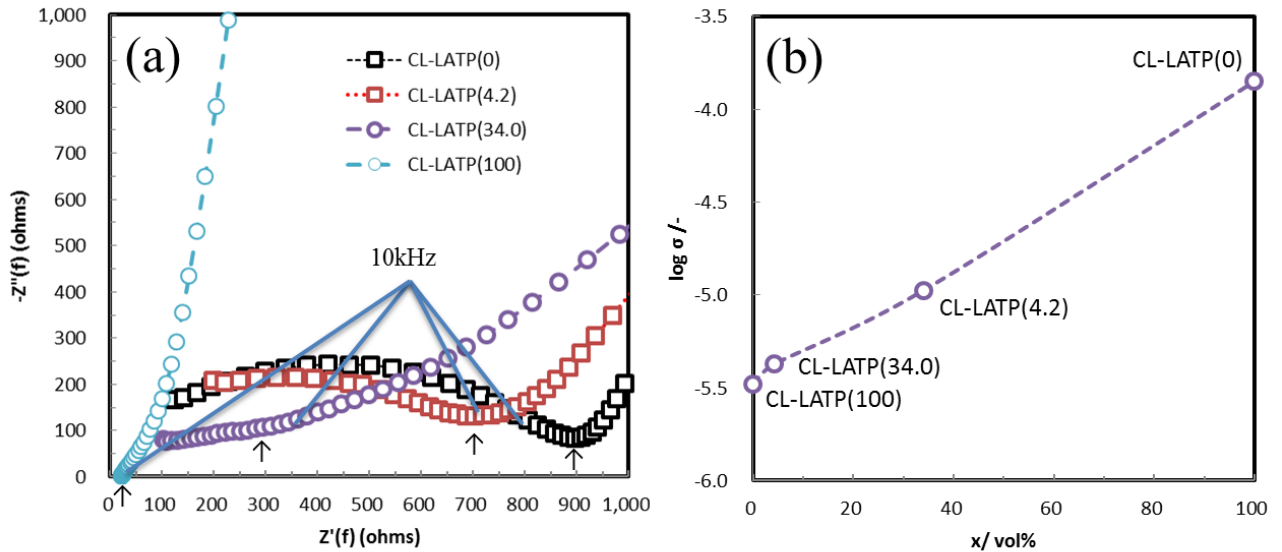mpedance spectroscopic measurements. The CL-LATP exhibited a high conductivity of 0.14 mS/cm at room temperature. By using conductivity spectra, the difference of the Li-ion transfer mechanism between CL-LATP and CL-ZrO$_2$ was also discussed. Their results suggest that the Li-ion conduction paths for CL-ZrO$_2$ and CL-LATP are mainly the PEO-LiTFSI (Path A) and the LATP particles (Path B), respectively. Moreover, in a future article, the usage of single-crystalline LATP or zirconium-based garnet electrolytes of Li$_7$La$_3$Zr$_2$O$_{12}$ (LLZO) should be developed into more practical conductivity. We will report on the performance of CLs and all-solid-state LIBs, as well as all-solid-state Li-air batteries.

2.5 References

[1] Abe T., Ohtsuka M., Sagane F., Iriyama Y., Ogumi Z., Soc. 151 (2004) A1950–A1953.
[2] Lee H., Yanilmaz M., Toprakci O., Fu K., Zhang X., Energy Environ. Sci. 7 (2014), 3857–3886
[3] Zhang X.-W., Wang C., Appleby A.J., Little F.E., J. Power Sources 112 (2002) 209–215.
[4] Yi J., Zhou H., ChemSusChem 9 (2016) 2391–2396.
[5] Bronstein L.M., Joo C., Karlinsey R., Ryder A., Zwanziger J.W., Chem. Mater. 13 (2001) 3678–3684.
[6] Aetukuri N.P.B., Hart M.W., Kim H., Kitajima S., Krupp L.E., McCloskey B.D., Miller R.D., Scott J.C., Wilcke W., US Patent 20150255767A1, filed March 6, 2014 and issued September 10, 2015.
[7] Zhang T., Imanishi N., Hasegawa S., Hirano A., Xie J., Takeda Y.,

Yamamoto O., Sammes N., J. Electrochem. Soc. 155 (2008) A965–A969.

[8] Shin J.H., Henderson W.A., Tizzani C., Passerini S., Jeong S.-S., Kim K.-W., J. Electrochem. Soc. 153 (2006) A1649–A1654.

[9] Arbi K., Hoelzel M., Kuhn A., García-Alvarado F., Sanz J., Chem. Chem. Phys. 16 (2014) 18397–18405.

[10] Kunshina G.B., Gromov O.G., Lokshin E.P., Kalinnikov V.T., J. Inorg. Chem. 59 (2014) 424–430.

[11] Kitaura H., Zhou H., Adv. Energy Mater. 2 (2012), 889–894.

[12] Chen B., Huang Z., Chen X., Zhao Y., Xu Q., Long P., Chen S., Xu X., Electrochim. Acta 210 (2016) 905–914.

[13] Arbi K., Bucheli W., Jiménez R., Sanz J., J. Eur. Ceram. Soc. 35 (2015) 1477–1484.

[14] Kiesow I., Marczewski D., Reinhardt L., Mühlmann M., Possiwan M., Goedel W. A., J. Am. Chem. Soc. 135 (2013) 4380.

3 Fabrication and impedance analysis for designed composite membranes with polymer and inorganic electrolytes

3.1 Introduction

The structure with the continuous pathway of LICPs from one side to another side in the membrane is effective not only in the inorganic-polymer electrolyte composites [1-3] but also in the inorganic electrolyte-insulating polymer composites [4]. We have fabricated the CLs, as mentioned in the chapter 2, where the mono-layered LICPs are uniformly embedded in the matrix of a polymer electrolyte. The surface of LICPs is covered with a polymer electrolyte. This means CLs have bulk resistance of the polymer and the polymer–LICP interfacial resistance.

To overcome these limitations, we designed and fabricated one-ceramic-particle thick LICP–polymer composite membranes wherein the LICP are circumferentially bound by a Li-ion insulating organic polymer matrix such that the top and bottom surfaces of the particles are not covered by the polymer. This geometry completely eliminates the high impedance inorganic–polymer and interparticle interfaces in the direction of Li-transport while rendering the membrane flexible and mechanically robust at small thicknesses (<100 μm) necessary for high Li-ion conductance. Furthermore, our approach does not require extensive particle pretreatment for particle functionalization or post deposition polymerization or crosslinking [5]. This procedure for making one-particle thick

membranes (OPTMs) is uniquely simple, versatile, and amenable for large-scale manufacturing.

3.2 Composite membranes-Generation 1

3.2.1 Experiments

3.2.1.1 Materials

The cyclo olefin polymer (COP), Zeonor 1060R, was purchased from Zeon Corporation, Japan. The glass transition temperature of this polymer was measured by modulated differential scanning calorimetry to be 103 ºC. The molecular weight was measured by static light scattering in cyclohexane solution and was found to be 22.4 kDa. The hydrodynamic radius as measured by dynamic light scattering in the same solution is 5.77 nm. Anhydrous cis+trans mixture of decahydronapthalene (decalin) was purchased from Sigma Aldrich. The adhesive tape (3M™ water-soluble wave solder tape 5414) was purchased from 3M™.

$Li_{1.6}Al_{0.5}Ti_{0.95}Ta_{0.5}(PO_4)_3$ (LATTP) glass-ceramic, which is one of NASICON-type LICCs, was prepared by induction melting of raw materials in a quartz crucible at 1500 °C – 1650 °C in air, as described previously [6]. The raw material composition (in weight %) is as follows: 5.4% Al_2O_3 (source: $Al(PO_3)_3$), 5.2% Li_2O (source: LiH_2PO_4), 45.9% P_2O_5 (source: LiH_2PO_4 and $Al(PO_3)_3$), 3.9% SiO_2, 23.2% Ta_2O_5 and 16.4% TiO_2. The melt was cast onto a metal plate forming glassy plates of 3 mm – 8 mm in thickness and 30 mm – 40 mm in diameter. Some of the glass was poured on a twin roller device to produce glass ribbons for powder production. The glass samples were annealed just below the glass

transition temperature at 530 ºC and slowly cooled to room temperature (rate 20 ºC/h). The resulting glass samples were dark, violet, with spontaneous crystallization occurring in few spots. Nucleation and crystallization temperatures were determined by differential thermal analysis and accordingly samples were annealed at 850-950 ºC for 12 hours and slowly cooled to room temperature to form the glass ceramic used for our experiments. The main phase has a NASICON structure with nominal composition of LATTP, isostructural to $LiGe_2(PO_4)_3$ and $LiTi_2(PO_4)_3$. SiO_2 (Cristobalite), observed as an impurity phase (<2 % by weight) in the XRD spectrum (Fig. 3-1(a)), is possibly formed during the heat treatment step.

For the preparation of Ta-doped $Li_7La_3Zr_2O_{12}$ (LLZO) ceramic powders, technical grade raw materials were mixed in the following proportions (in weight %): 13.9 % Li_2O, 53.6% La_2O_3, 20.3% ZrO_2 and 12.1wt% Ta_2O_5. Since this composition is highly 22 corrosive, skull melting technology, as previously described [7], was used. This technique uses a water cooled crucible (skull crucible) leading to the formation of a barrier layer of solidified melt between crucible and melt. The batch was preheated using a gas burner, then melted using high frequency induction heating. After stirring and homogenizing the melt, the induction heating was switched off, allowing the melt to cool slowly to room temperature. The resulting material was white- to slightly yellow-colored and highly crystalline with 100 % cubic garnet crystalline phase (as determined by XRD). No impurity phases were detected. Bulk samples and powder material were prepared from the crystallized ingot using water-free preparation methods.

3.2.1.2 Composite membranes-Generation 1 of Preparation Procedure

LATTP powders, with particle sizes <150 μm, are sieved using ASTM standard sieves to obtain a narrow size distribution. Particles in the size ranges of 75-90 μm, 63-75 μm or 45-53 μm are used for the preparation of the composite membranes-Generation 1 (OPTM-Gen1). A commercially available COP is chosen for the matrix as it possesses very low electronic and Li-ion conductance, is thermally stable up to its glass-transition temperature of ~105 ºC and is found to have immeasurably low solubility and swelling (increase in volume due to solvent absorption) in most battery electrolyte solvents. It is also amorphous after spin casting needing no further treatment and therefore simplifies the membrane preparation process. A schematic of the process used for the preparation of the membranes is shown in Fig. 3-2(a). Sieved particles are dispersed and gently pressed onto a tape with an ethanol soluble adhesive (ESA). The tape along with the particles is heated to a temperature of 130 ºC, which thermally contracts the tape. This step improves the particle packing density and eliminates any thermal stresses in the latter steps that involve heating. Next, an 8 wt% solution of COP in decalin (the solvent) is spin-casted 5 times at 90 ºC on the particles' assembly. This forms a continuous polymer matrix around the particles after the solvent is allowed to evaporate at 130 ºC for 4 hours. In addition, COP redistributes at this temperature to form a uniformly thick coating, which also covers the top surface of the particles. The excess polymer on the particles' top surfaces is then removed by etching in a dry reactive oxygen plasma for <5 min. Finally, the OPTM-Gen1 is detached from the tape

using a lift-off technique wherein the ESA is slowly dissolved (over 3 days) in ethanol at 70 ℃. Excess ethanol on the membrane is evaporated by drying in ambient conditions. The membranes are further dried at 80 ℃ overnight before being used for experiments. SEM micrographs of the cross-section are shown in Fig. 3-2(b) and the plane views of the top (air side) and bottom (adhesive side) surfaces of a typical membrane are shown in Fig. 3-2(c). Nearly mono-disperse LATTP powder particles can be clearly seen. These membranes, as prepared, are highly flexible as exemplified with a membrane wrapped around a standard HB pencil (see Fig. 3-2(d)).
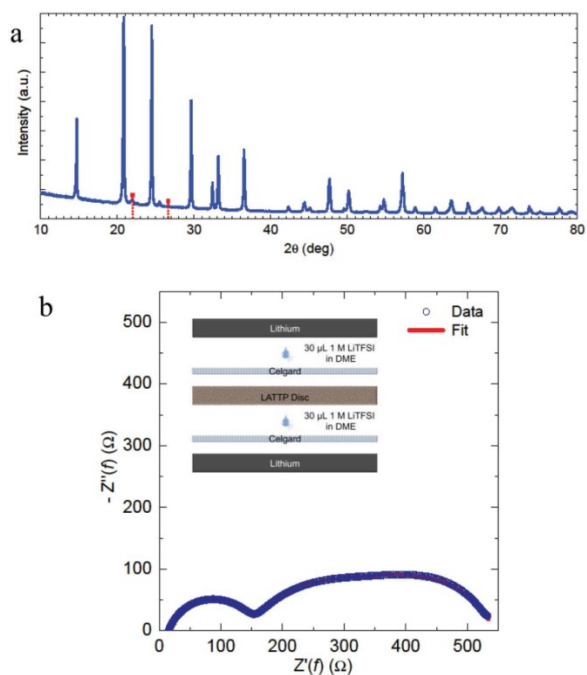
Fig. 3-1. (a) Typical XRD spectrum of LATTP ceramic. Except for a very tiny fraction of cristobalite (corresponding peaks identified as vertical red dotted lines), all peaks can be indexed to NASICON-type LATTP. (b) Nyquist plot of the impedance data for a 500 μm thick LATTP disc measured with symmetric Li electrodes. The three characteristic semicircles observable in the impedance curve are attributed to intragrain impedance and grain boundary impedance of LATTP, and the impedance of SEI on the Li electrodes (Fig. 3-3 and Table 3-1). The inset shows the schematic arrangement of the components in the symmetric cell used for impedance measurements. The components are separated for clarity.

48
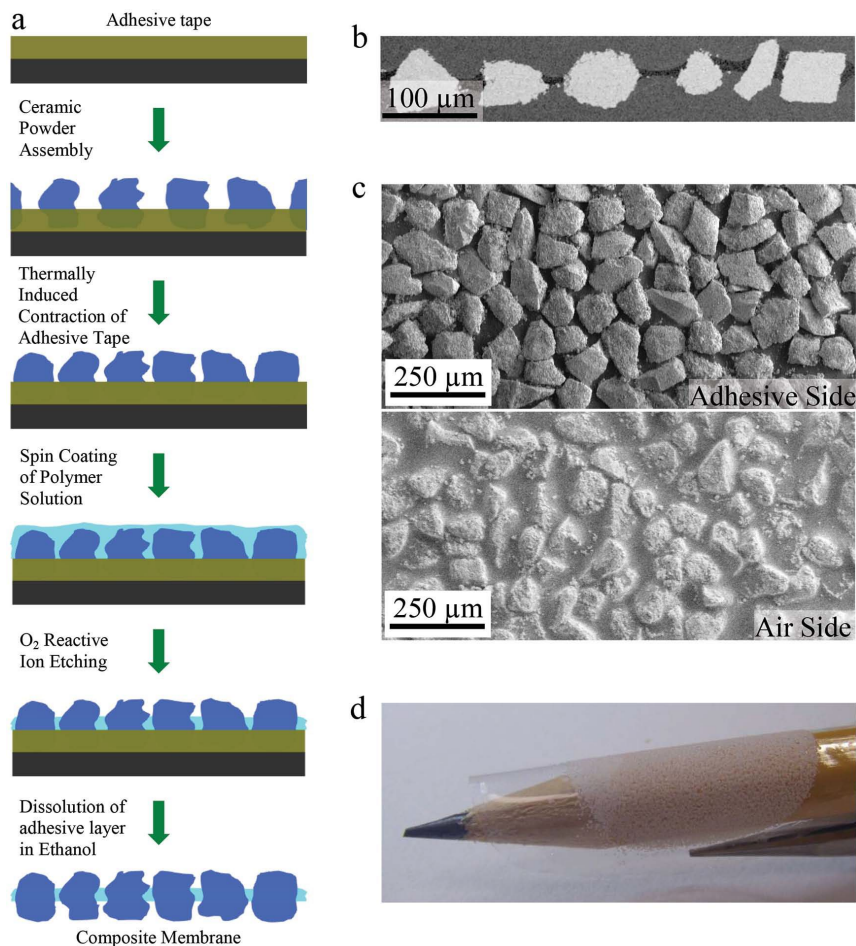
Fig. 3-2. (a) A schematic of the steps involved in the fabrication of OPTM-Gen1. (b) Cross-sectional SEM microscopy image of a typical membrane (width of the image is equivalent to 500 μm). Note that the epoxy (gray) used for sample mounting is seen on either side of the particles and the COP (dark gray) that binds the LATTP particles (light gray) is contrast enhanced to differentiate it from the epoxy. (c) Plane-view SEM images of the adhesive side and the air side of the OPTM-Gen1 showing nearly mono disperse LATTP ceramic particles. Image width is 1.28 mm. d) An optical photograph of the composite membrane wrapped around a standard HB pencil. The high flexibility is typical of all the membranes developed in this work.

3.2.1.3 Reactive-ion etching

Reactive-ion etching was performed in a commercial Plasma-Therm Versaline etcher operating at a coil power of 600 W and a platen power of 10 W. The oxygen flow rate and pressure during etching are 50 sccm and 20 mTorr respectively. The membranes for etching are mounted on a silicon substrate which is loaded on to a water cooled substrate holder in the ion-etcher. COP etch rate under these conditions is 1.6 µm per minute.

3.2.1.4 Scanning electron microscopy

For cross-section SEM measurements, the membranes were embedded in G-1 epoxy (Gatan, Inc.) and outgassed under vacuum for 1 hour prior to curing at 80 ºC for 2 hours between 2 glass coverslips with no pressure applied. They were cross-section polished on an Allied High Tech Multi-Prep using Buehler diamond films and an alcohol-based polishing suspension (Purple Lube, Allied High Tech). The cross sections are coated with 5 nm carbon in a Cressington 208C coater prior to SEM imaging in a FEI Helios Nanolab 400S FIB/SEM.

3.2.1.5 Impedance measurements

Li electrodes are used for Li-ion impedance measurements. OPTM-Gen1 or ceramic discs are separated from the Li electrodes using a Celgard separator wetted in liquid electrolyte (1 M LiTFSI in DME). Small signal (V_{p-p} = 10 mV) AC impedance 25 measurements are performed on an Agilent 4294A impedance analyzer using sinusoidal AC

waveform in the frequency range of 40 Hz to 110 MHz. To separate the various contributions to the measured impedance, the impedance spectra are simulated by an equivalent circuit as given in Fig. 3-3. Solid electrolyte interphase (SEI), the intra-grain (IG) which means the bulk and the grain boundary (GB) impedances are considered. These three components are modeled to be in series and each component is a parallel combination of a resistive element (R) and a constant phase element, $Q = C_{1/n}$ [8]. The governing equation used for simulating the experimental data is given by equation in Fig. 3-3. The results of this analysis are compared to frequency analysis before impedance assignment to each of the three components modeled. A summary of the results are tabulated in Tables 3-1, Table 3-2 and Table3-3.

3.2.2 Results and Discussion

3.2.2.1 Li-ion-Conducting Ceramic Characterization

$Li_{1.5}AlGe_{1.5}(PO_4)_3$ (LAGP) is also one of the most widely studied Li-ion-conducting compounds that have the NASICON-type crystal structure [9]. However, germanium is a costly element. We therefore developed a new germanium-free $Li_{1.6}Al_{0.5}Ti_{0.95}Ta_{0.5}(PO_4)_3$ (LATTP) compound as a cost-effective alternative to the LAGP materials. LATTP is also one of the Li-analogues of the NASICON-type Li-ion-conducting compounds [10]. It is prepared by standard melting and crystallization techniques. A typical X-ray diffraction (XRD) plot for this material is shown in Fig. 3-1(a). The XRD shows that the material is polycrystalline with a negligibly small impurity phase of cristobalite (a hightemperature

polymorph of SiO_2). A 500 μm thick × 12 mm diameter disc of this material is used for impedance measurements to ascertain the Li-ion-conducting properties. Measurements are performed using a symmetric Li electrode configuration connected to stainless steel current collectors. A liquid lithium electrolyte (inset of Fig. 3-1(b)) is used between the ceramic disc and the lithium electrodes on either side for improved electrical contact. A typical Nyquist impedance plot is shown in Fig. 3-1(b). Based on equivalent circuit analysis, there are at least three characteristic semicircles in this Nyquist plot that are attributed to: (1) Intragrain impedance (intragrain resistance: 127 Ω), (2) grain boundary impedance (grain boundary resistance: 212 Ω), and (3) the impedance due to the formation of a solid electrolyte interphase (SEI) on the metallic Li surface (SEI resistance: 185 Ω) (Table 3-1, and Fig. 3-3). The net conductivity for this disc (≈0.1 mS/cm) is comparable to Li-ion conductivities in similar classes of compounds [11,12]. Of particular note is the intragrain conductivity of ≈0.3 mS/cm which approaches the best reported values for these compounds [10]. We used this highly conducting LATTP material in powder form for the fabrication of OPTMs, as explained below.

$$Z = \frac{R}{1+i(\omega RC)^n}$$
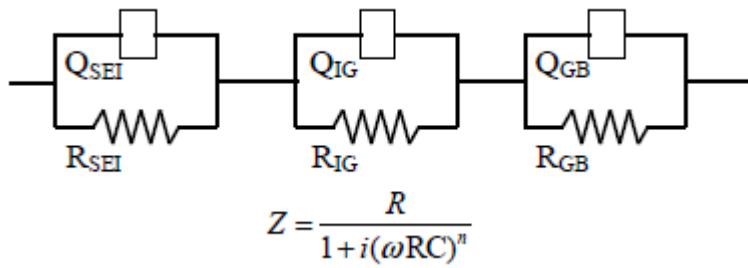
Fig. 3-3. Equivalent circuit model used for simulating the experimentally obtained impedance data.

Table 3-1. Summary of parameters from the equivalent circuit model for the LATTP ceramic disc.

Element	R (Ω)	C (nF)	n
Intra Grain	127 ± 0.95	0.13 ± 0.001	0.86 ± 0.005
Grain Boundary	212 ± 6.61	47.5 ± 0.69	0.674 ± 0.008
Solid electrolyte Interphase	185 ± 6.38	971 ± 61.4	0.765 ± 0.008

3.2.2.2 Li-ion Impedance of Composite membranes-Generation 1

A typical Nyquist plot of the impedance data for the OPTM-Gen1 (1/2" diameter), Fig. 3-4, shows three characteristic semi-circles similar to the Nyquist plot for the LATTP disc (Fig. 3-1(b)). For this membrane, based on equivalent circuit analysis, the intra-grain resistance is ~24 Ω, the grain boundary resistance is ~104 Ω and the SEI resistance is ~76Ω. We note that the electronic conduction, if any, in these OPTM-Gen1 is below our measurement threshold (<1 nΩ). By comparing this to the impedance data of the ceramic disc, we can conclude that the Li-ion conductance of these membranes is much higher than that of solid ceramic discs. For example, the total intra-grain resistance, which scales monotonically with the thickness of the ceramic particles, is approximately 5.5 times lower than that of the LATTP disc. This is consistent with the disc being approximately 5.5 times thicker than the membrane (~75-90 μm diameter particles compared to ~500 μm thickness of the disc). While this decrease in resistance is not surprising, we note that a thinner, 75 μm thick, ceramic disc will be too brittle to be of any practical use. On the other hand, the polymer matrix of the OPTM-Gen1 makes them flexible and usable even when they are very thin. As a result, high Li-ion conductance is achieved in these novel OPTM-Gen1, without compromising the highly desirable mechanical integrity of the film.
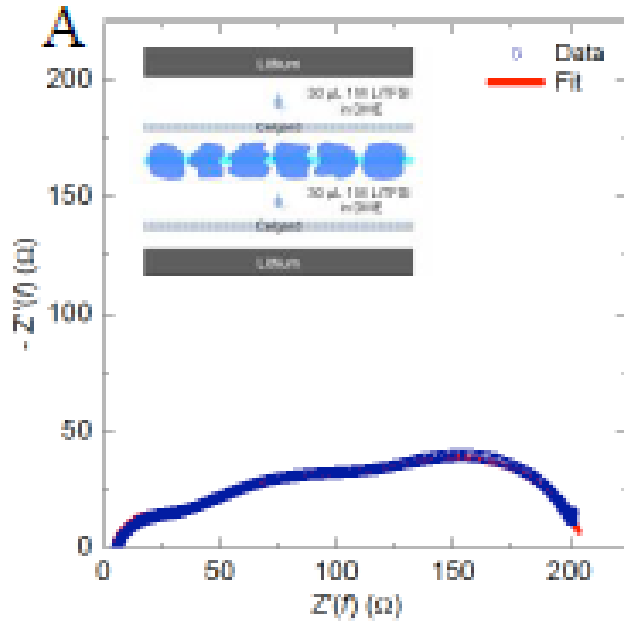
Fig. 3-4. Nyquist plot of the impedance data for a typical OPTM-Gen1 prepared from 75−90 μm thick LATTP particles measured with symmetric Li electrodes. The resistances extracted by fitting the experimental data are: intra-grain resistance = 24 Ω, grain-boundary resistance = 104 Ω, SEI resistance = 76 Ω (Table 3-2). The inset shows the schematic arrangement of the components in the symmetric cell used for impedance measurements. The components are separated for clarity.

Table 3-2. Summary of parameters from the equivalent circuit model for the LATTP based OPTM-Gen1.

Element	R (Ω)	C (nF)	n
Intra Grain	24 ± 1	0.86 ± 0.01	0.87 ± 0.01
Grain Boundary	104 ± 2	24.7 ± 0.4	0.60 ± 0.01
Solid electrolyte Interphase	76 ± 2	1160 ± 40	0.84 ± 0.01

Extending our approach to another ceramic material, we prepared LLZO-based OPTM-Gen1 following a procedure similar to that described for LATTP-based OPTM-Gen1. These membranes showed impedance characteristics similar to LATTP membranes (Fig. 3-5).
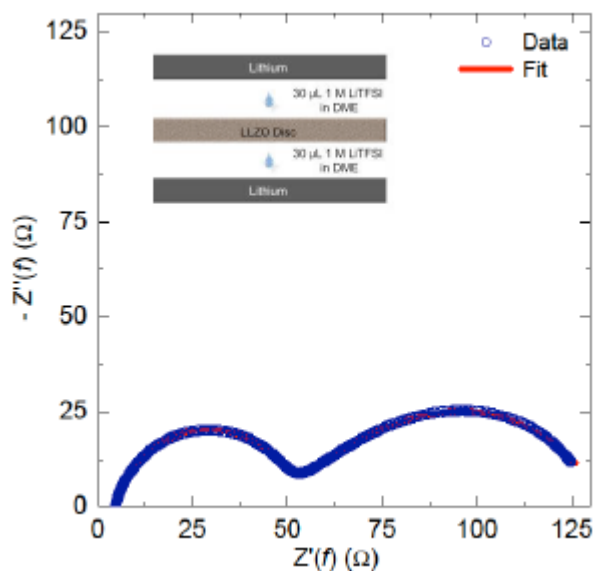
Fig. 3-5. Nyquist plot for a typical LLZO-based OPTM-Gen1 prepared from 75-90 μm thick LLZO particles measured with symmetric Li electrodes. The summary of the simulations to the experimental data is shown in Table. 3-3.

Table 3-3. Summary of parameters from the equivalent circuit model for LLZO-based OPTM-Gen1.

Element	R (Ω)	C (nF)	n
Intra Grain	45 ± 0.09	1.71 ± 0.003	0.90 ± 0.001
Grain Boundary	76.4 ± 0.95	810 ± .004	0.61 ± 0.003
Solid electrolyte Interphase	10 ± 0.95	9900 ± 0.98	1.07 ± 0.02

3.3 Composite membranes-Generation 2

3.3.1 Experiments

3.3.1.1 Materials

$Li_{1.3}Al_{0.3}Ti_{1.7}P_3O_{12}$ (LATP) was chosen from the viewpoint of its high Li-ion conductivity and stability in ambient air. The LATP particles (LATP, Toshima Manufacturing Co., Ltd.) were sieved from 38 μm to 45 μm-sized particles and from 20 μm to 25 μm-sized particles. The composite membranes (OPTM-Gen2) using the larger particles with the range from 38 μm to 45 μm are used as the standard sample of this report and written as LP-RIE-y. Furthermore, the smaller particles with the range from 20 μm to 25 μm were used to decrease the thickness of OPTM-Gen2. The abbreviation of OPTM-Gen2 with the smaller particles is SP-RIE-y. The variable number of y in LP-RIE-y and SP-RIE-y is etching time mentioned in the following section. Through process optimization, 50 μm-sized ZrO_2-based insulating particles (Niimi NZ beads 50, Niimi Sangyo) were used to optimize the fabrication of OPTM-Gen2. As the matrix polymer of OPTM-Gen2 as well, like OPTM-Gen1, a COP (Zeonor 1060R) was purchased from Zeon Corporation, Japan. The glass transition temperature of this polymer was determined to be 103 ºC by modulated differential scanning calorimetry.
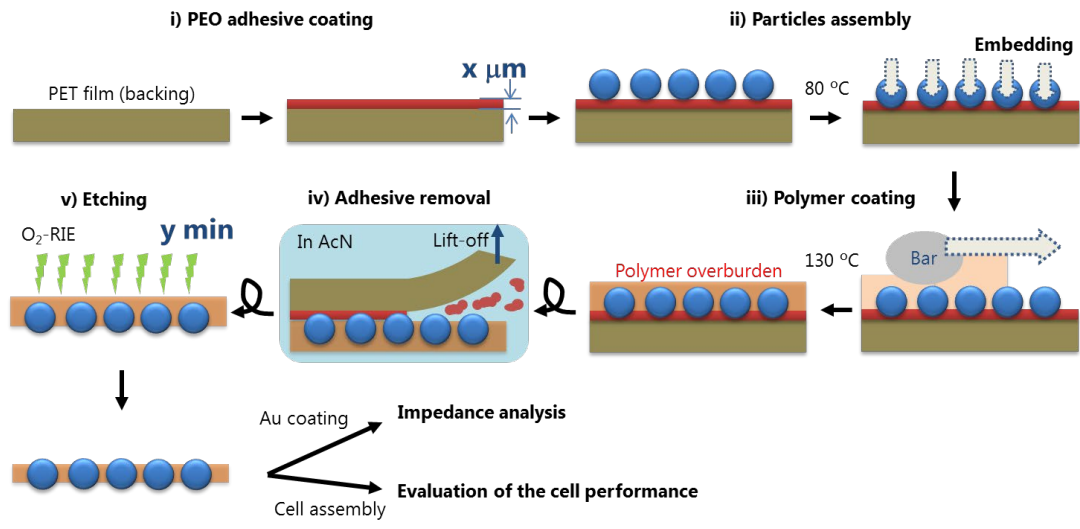
Fig. 3-6. Fabrication of an OPTM-Gen2: Schematic of the steps involved in the revised fabrication of OPTM-Gen1.
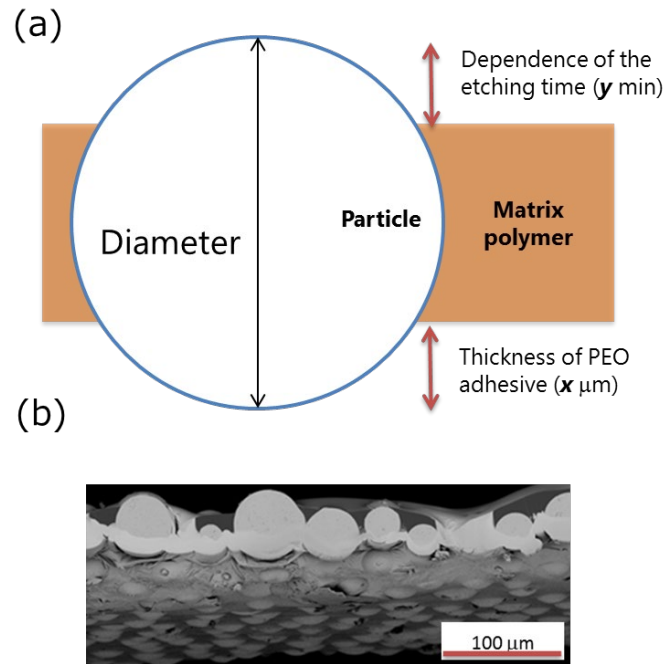
Fig. 3-7. Modeling using 50 μm-sized ZrO_2-based particles instead of LATP particles: (a) the design for OPTMs with 2 important parameters: the thickness of the PEO adhesive (x) and the etching time (y) correlating with the thickness of the etched portion, (b) tilted cross-sectional SEM image of a model-OPTM employing 50 μm-sized ZrO_2-based particles for confirming the state of the polymer matrix and exposed particles on the adhesive side at same time. The thickness of the PEO adhesive (x μm) was standardized to approximately 10% of the particle diameter: approximately 4 μm in case of 38 to 45 μm-sized particles and approximately 2 μm in case of 20 to 25 μm-sized particles.

3.3.1.2 Fabrication of Composite membranes-Generation 2

A schematic of the fabrication process of the OPTM-Gen2 via a revised procedure based on the previous one is shown in Fig. 3-6. In the previous process of OPTM-Gen1,

commercial masking tape was used to cover the bottom side of the particles. Since moisture is adsorbed on the adhesive of the masking tape, the thickness and softness change depending on conditions. Therefore, the embedding of the particles is not uniform, and it also makes adjustment of the following steps difficult. In this process, we made masking tapes to avoid the moisture adsorption. It provides not only adjustable process but also a suitable thickness of the adhesive layer. In addition, the condition of oxygen dry reactive ion etching (O_2-RIE) was moderated to control the thickness of polymer matrix more properly. The present process was advanced in the 5 steps described below to obtain the OPTM-Gen2 with higher conductivities than the previously reported one [13] and OPTM-Gen1.

i)   PEO without salt is hard and non-adhesive, however, interestingly, the addition of the electrolyte salt rendered the film tacky enough to retain LICPs [13]. Lithium(bistrifluoromethanesulfonyl)imide (LiTFSI) was used as a salt. PEO (Mw = 600,000) was mixed with LiTFSI with the weight ratio of 18 : 1 in the acetonitrile (AcN) solvent. The PEO-LiTFSI solution was applied onto a backing film of polyethylene terephthalate (PET) by the bar-coating. Then the film was dried at 80 °C and an adhesive thin film was obtained. Hereafter the adhesive layer is called PEO adhesive. The thickness of the PEO adhesive (x μm) was determined to approximately 10% of the particle diameter, as described in Fig. 3-7. The value of x was controlled by the speed of bar-coating.

ii)   Well-sieved particles were distributed on the PEO adhesive surface and the excess

particles were removed by shaking. This process was repeated several times until good particle coverage was achieved and adsorbed particles were then gently pressed onto PEO adhesive heated to 80 ºC (above T_m of PEO) to embed the particles into the PEO adhesive.

iii)   Next, a 16 wt% solution of COP in decalin (the solvent) was bar-coated on the particle assembly. The clearance of bar-coating was determined to be ~6 times thicker than the average particle size; 250 μm in case of 38 to 45 μm-sized particles and 135 μm in case of 20 to 25 μm-sized particles. This yielded a continuous polymer matrix around the particles after the solvent is evaporated at 130 °C over 3 h.

iv)   The OPTM-Gen2 was detached from the PEO adhesive using a lift-off technique. The stacked film was soaked into AcN at room temperature. After the PEO adhesive was dissolved, the masking tape was removed from the OPTM-Gen2. Then the membrane was dried in an ambient condition to evaporate the remaining AcN. Under these conditions, the particles on the PEO adhesive side (adhesive side) were not coated with COP.

v)   The polymer overburdened on the opposite side (polymer side) can be removed via O_2-RIE for an appropriate time. O_2-RIE was performed in a commercial Oxford plasmalab 100 series ICP-RIE system at a coil power of 0 W and a platen power of 100 W. The oxygen flow rate and pressure during etching were 100 sccm and 30 mTorr, respectively. Importantly, the sufficient polymer matrix has to be remained,

for example, so that short-circuit is not produced by coating with gold (Au) for electrical measurements.

3.3.1.3 Impedance analysis

For comparison, a commercial LATP disc (LICGC^{TM} AG-01) was purchased by OHARA inc., Japan. We evaluated the ionic conductivities of OPTM-Gen2 and the commercial LATP disc from AC impedance measurements performed on the gold coated sandwich structure (Au/sample/Au). Au was sputtered on the sample surfaces in an argon gas flow for making good contact between Au and samples. We collected AC impedance spectra using a potentiostat (VMP3, Bio-Logic) in the frequency range of 1 Hz to 1 MHz with a perturbation voltage of 10 mV. Impedance measurements were performed at the temperatures between −10 °C and 80 °C, which is controlled by using a thermostatic oven (ESPEC). The ionic conductivity σ was calculated using the following equation:

$$\sigma = d/(R \times S) \qquad (1)$$

where, d is the thickness of the OPTM-Gen2, R is the resistance obtained from Nyquist plots, and S is the area of Au electrode. Here, the average particle size (41.5 μm for 38 to 45 μm-sized particles and 22.5 μm for 20 to 25 μm-sized particles) was used as the thickness of the OPTM-Gen2. Further, the activation energy was calculated from the Arrhenius plot by fitting with the Arrhenius equation:

$$\sigma = A \, exp(−E_a/kT) \qquad (2)$$

where, A is a pre-exponential factor, E_a is the activation energy, T is the absolute

temperature, and k is the Boltzmann's constant.

3.3.2 Results and Discussion

3.3.2.1 Design of Composite membranes-Generation 2

In the designing of OPTM-Gen2, the exposure condition of LATP particles from the matrix polymer and thickness of the matrix polymer are important factors. The conductivity of OPTM-Gen2 would increase with an increase in the exposure of LATP particles. In contrast, the sufficient thickness of the matrix polymer prevents from forming the through-holes or cracking, and provides the excellent handleability and processability. In the present process, these factors were controlled by the two parameters of the thickness of PEO adhesive (x μm) and etching time (y min).

First, the OPTM-Gen2 using the larger particles with the range from 38 μm to 45 μm were prepared with varying etching time (y min). The thickness of PEO adhesive (x μm) was controlled to approximately 4μm as determined in Fig. 3-7. Fig. 3-8 shows the plane-view SEM images for the etching side of OPTM-Gen2 after various O_2-RIE treatment times. The no etching sample (LP-RIE-0) in Fig. 3-8 (a) shows the flat surface completely covered with COP. After etching for 40 min (LP-RIE-40), small islands of LATP particles exposed from the polymer matrix were observed in Fig. 3-8 (b). In the LP-RIE-120, the etching for 120min provides the highly exposed area of LATP particles as shown in Fig. 3-8 (c). Fig. 3-8 (d) demonstrates the cross-sectional SEM image of LP-RIE-120. It was observed that a sufficient thickness of matrix polymer without any

through-holes or cracks is retained in this condition. As additional discussion, we added the enlarged SEM image (red boxed image) as shown in Fig. 3-8 (c). The bristle brush-shaped structure was confirmed in this image of LP-RIE-120. The discussion about this structural object will be described in combination with XPS analysis inChapter 4.
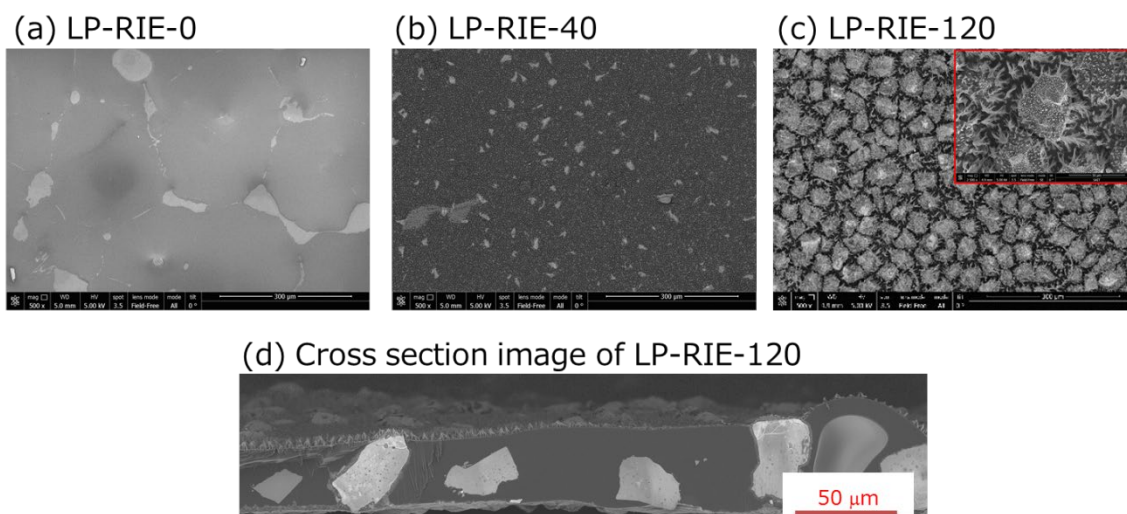
Fig. 3-8. Plane-view SEM images for the polymer side of OPTM-Gen2 at various O_2-RIE treatment times: (a) LP-RIE-0 (unetched sample), (b) LP-RIE-40, and (c) LP-RIE-120. (d) Cross-sectional SEM image of LP-RIE-120 (upper side is the polymer side). Ion laser was used to prepare the cross-sectional sample.

3.3.2.2 Nyquist plots

Impedance behaviors of LP-RIE-40 and LP-RIE-120 were investigated at different temperature in comparison with those of a commercial LATP disc. Fig. 3-9 displays typical Nyquist plots obtained at various temperatures from -10 ℃ to 80 ℃ for LP-RIE-40 and LP-RIE-120. For the comparison, Fig. 3-10 shows Nyquist plots of a commercial LATP

disc. The large semicircle shown in Fig. 3-10 can be ascribed to the grain boundary resistance of the LATP disc and the near-vertical line is related to the electrode polarization of the blocking electrode. On the other hand, no clear semicircle was observed in both OPTM-Gen2 at any temperatures. Therefore, the total resistances of the OPTM-Gen2 were estimated from the intercept of the near-vertical line with the real axis. The conductivities were calculated by using these values and partially summarized in Table 3-1. The reference data of typical type of LATP discs and the conductivity of the CLs we have reported were also listed in the table. The conductivities of LP-RIE-120 are much higher than those of LP-RIE-40, the various types of LATP disc and the CLs around room temperature as well as at −10 °C. The conductivities of 0.53 mS/cm at 20 °C and 0.22 mS/cm at -10 °C for LP-RIE-120 are approximately 6 and 15 times higher, respectively, than those for the commercial LATP sintered disc. In addition, the room temperature conductivity is the highest value among OPTM-Gen2 including previously reported ones [1, 13]. These results demonstrate that our revised fabrication process can lead to high Li-ion conductivity.
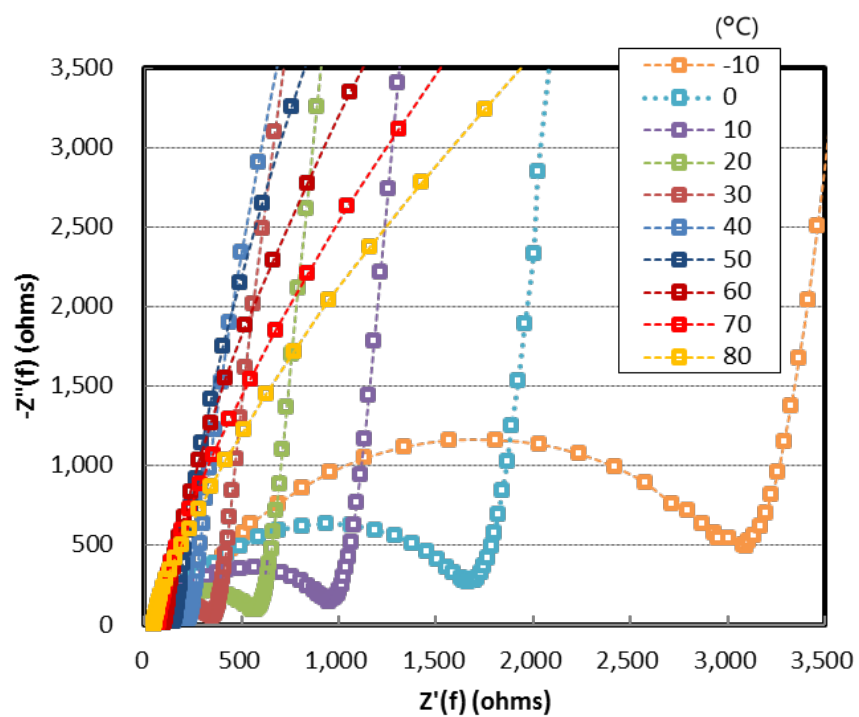
Fig. 3-10. Nyquist plots of the impedance data for Au/commercial LATP disc/Au at different temperatures.

Table 3-3. Conductivities of OPTM-Gen2, LATP disc and CLs at −10 °C, 20 °C and 30 ºC.

Temperature	OPTM-Gen2		LATP disc		CLs
	LP-RIE-40	LP-RIE-120	Commercial LATP disc	General LATP disc [14]	
-10 °C	0.07	0.22	0.015	-	0.0016
20 °C	0.19	0.53	0.09	1.2 - 3.1 (bulk)	0.14
				0.071 - 0.45 (total)	
30 °C	0.24	0.73	0.14	(27 °C)	0.31

[unit: mS/cm]
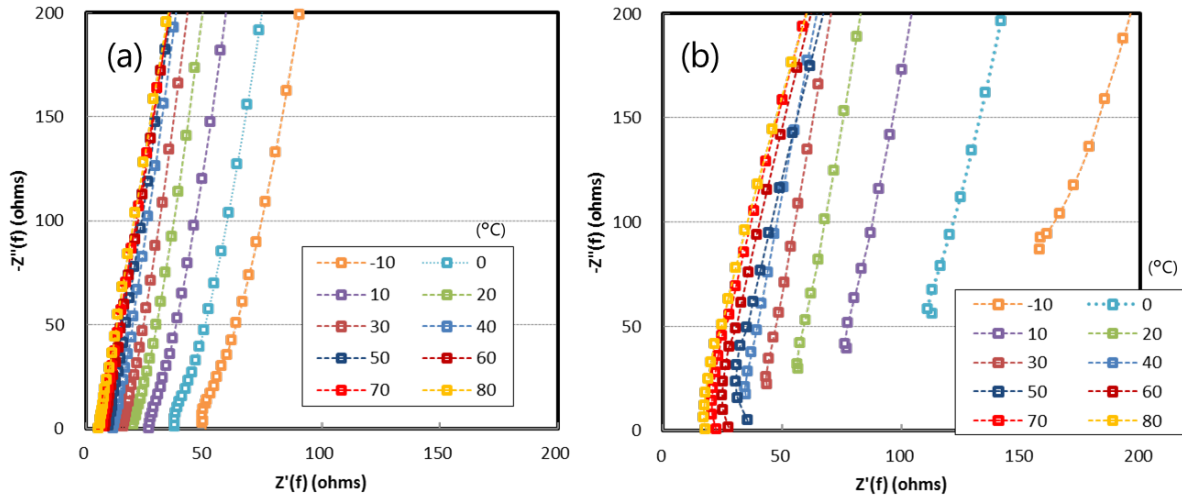
Fig. 3-9. Nyquist plots of the impedance data at various temperatures: (a) Au/LP-RIE-120/Au and (b) Au/LP-RIE-40/Au.

Then, the frequency dependence of the impedance changes was investigated. Conductivity spectra, i.e., the real part of the complex conductivity (σ) plotted vs. the frequency (log F), for the OPTM-Gen2 and the commercial LATP disc, are shown in Fig. 3-11 and Fig. 3-12, respectively. Electrode polarizations are seen due to the ion blocking electrode in the lower frequency. A near-flat area (DC plateaus), in case of the commercial LATP disc, is observed in Fig. 3-12. The frequency range of the DC plateaus gradually changed from the region of 40 Hz - 40 kHz at –10 °C to the region of 5 kHz - 1 MHz at 80 °C. These plateaus are due to Li-ion conduction through the grain boundaries [15]. In Fig. 3-11, conductivity spectra are shown for OPTM-Gen2. In contrast, the DC plateaus are

68

not seen in the same frequency ranges as Fig. 3-12. These results of Nyquist plots (Fig. 3-9) and the frequency dependence (Fig. 3-11) indicate that the drastic decrease of the grain boundary resistance component of OPTM-Gen2 might be derived from no or less grain boundaries.
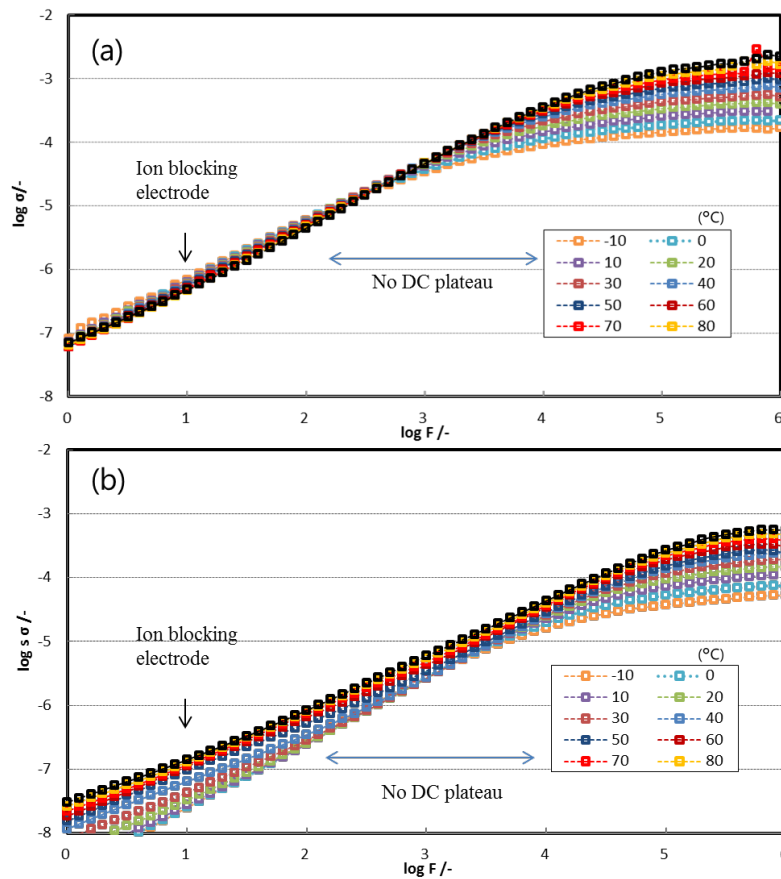
Fig. 3-11. Conductivity isotherms for OPTM-Gen2 at various temperatures:
(a) Au/LP-RIE-120/Au and (b) Au/ LP -RIE-40/Au.
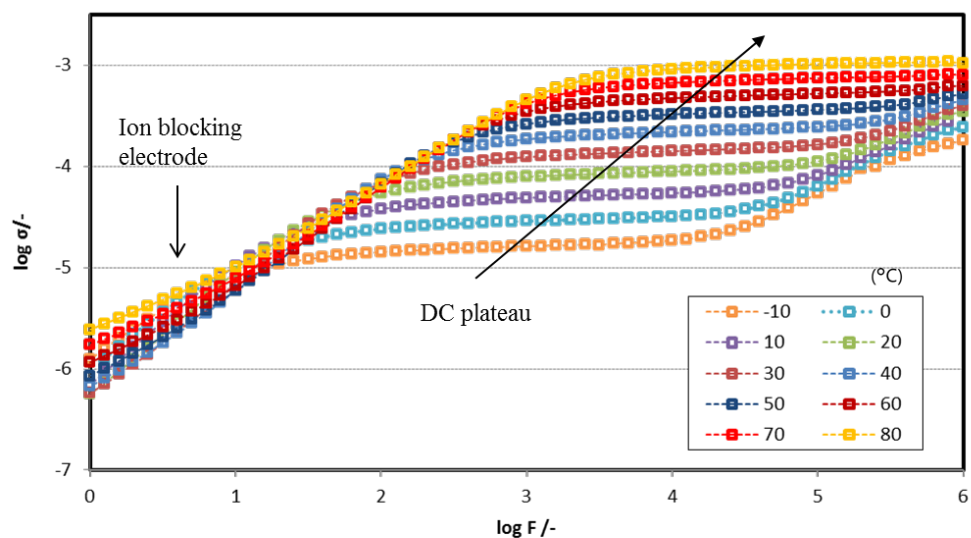
Fig. 3-12. Conductivity isotherms for Au/commercial LATP disc/Au at different temperatures.

Table 3-4. Activation energies of OPTM-Gen2, LATP disc and CLs.

	OPTM-Gen2		LATP disc		CLs
	LP -RIE-40	LP -RIE-120	Commercial LATP disc	General LATP disc [14]	
Activation energy	17.8	17.2	37.0	12.5 - 18.2 (bulk) 26.7 - 33.6 (total)	70.7

[unit: kJ/mol]

70

3.3.2.3 Arrhenius plots

The drastic decrease of the grain boundary resistance of OPTMs is also indicated by the activation energy calculated from the Arrhenius plots. Fig. 3-13 shows the temperature dependence of ionic conductivity for OPTM-Gen2. The data of CLs are also shown in the same figure by way of comparison. In addition, the activation energies, which were calculated by the total resistance of the OPTM-Gen2, the commercial LATP disc and the CLs, are summarized in Table. 3-4. The reference data calculated by bulk resistances and total resistances of typical type of LATP discs were also listed in the table. OPTM-Gen2 show not only higher Li-ion conductivities but also lower activation energies than the various types of LATP discs and the CLs. Importantly, the activation energy of LP-RIE-120 is 17.2 kJ/mol, which is in agreement with the activation energy of the bulk (inner crystal) of LATP reported previously [15]. This indicates that the conduction in the bulk (inner crystal) mainly governs the Li-ion conduction of OPTM-Gen2, although it should be still limited to some extent by the presence of some natural grain boundaries.
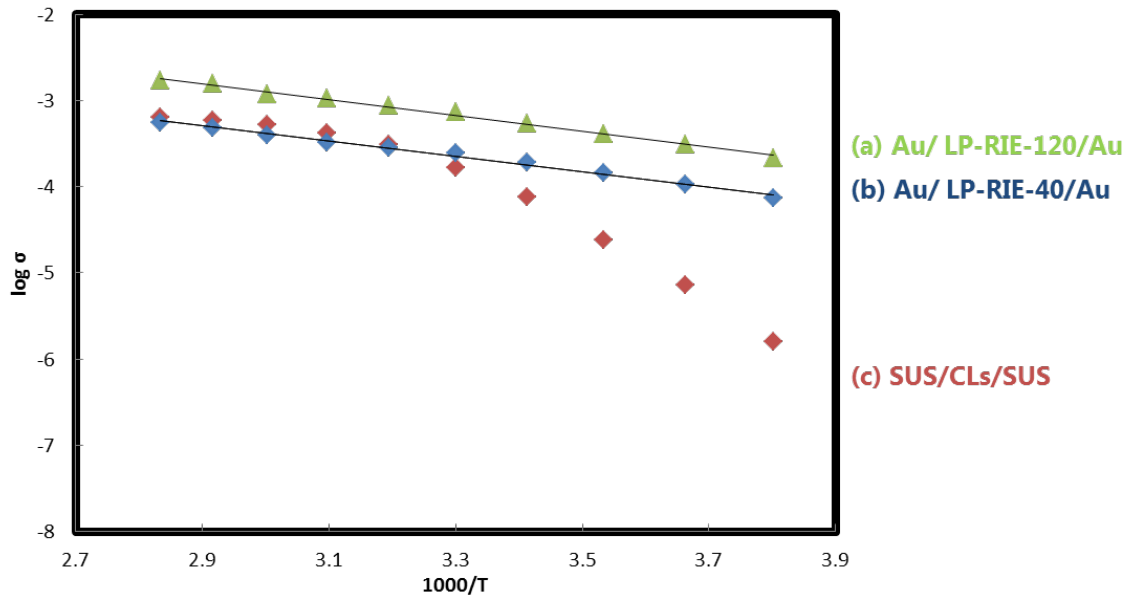
Fig. 3-13. Arrhenius plots for (a) Au/ LP-RIE-120/Au, (b) Au/ LP-RIE-40/Au, and (c) SUS/CLs/SUS.
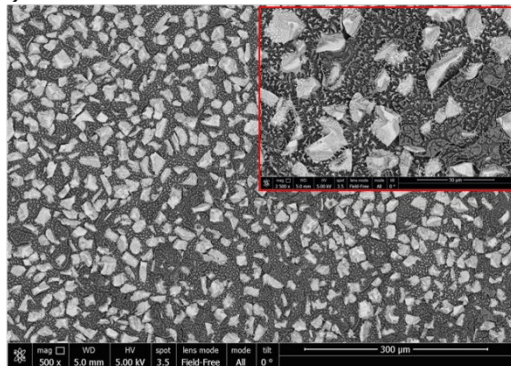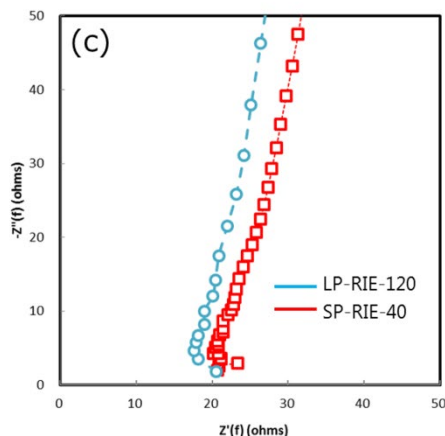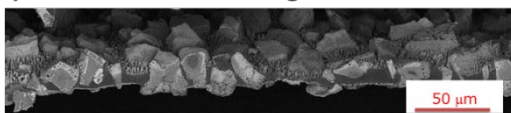
Fig. 3-14. (a) Plane-view SEM images for the polymer side of SP-RIE-40, (b) cross-sectional SEM image of SP-RIE-40 (upper side is polymer side), and (c) Nyquist plots of the impedance data of Au/ LP-RIE-120/Au and Au/SP-RIE-40/Au.

3.3.2.4 Thinned Composite membranes-Generation 2

It is very critical issue to make the solid electrolyte layer thinner for the purpose of the increasing the energy/power density. In the present method controlling the thickness of polymer matrix more properly, thinner OPTM-Gen2 can be prepared. A thinned OPTM-Gen2 was prepared by using the smaller particles (20 - 25 μm) and etching for 40 min (SP-RIE-40). Fig. 3-14 shows the SEM images of SP-RIE-40 and the Nyquist plots of SP-RIE-40 and LP-RIE-120 at 20 °C. The plane-view and the cross-sectional SEM images (Fig.3-14 (a) and (b), respectively) indicated that SP-RIE-40 has the exposed LATP surface with a relatively large area and the matrix polymer without through-holes or cracks under

73

this condition. However, the exposed area of SP-RIE-40 (Fig. 3-14(a)) is obviously lower than LP-RIE-120 (Fig. 3-8(a)). The resistance of SP-RIE-40 is almost the same as that of LP-RIE-120 as shown in Fig. 3-14 (c). This is consistent with the 3-dimensional geometry of each OPTM-Gen2. The area of the particle exposure of SP-RIE-40 is smaller but the thickness of the membrane is approximately 50% lower than LP-RIE-120. Therefore, the Li-ion conductivity of SP-RIE-40 is about 0.22 mS/cm, which is smaller than that of LP-RIE-120, but the total resistance becomes almost the same.

3.4   Conclusion

In summary, we have demonstrated a simple route for fabricating flexible Li-ion-conducting OPTMs with high Li-ion conductance and vastly improved mechanical properties relative to LICC disks of comparable thicknesses. This configuration eliminates the highly resistive interparticle ionic conduction pathways characteristic of multiparticle thick composites. Although our initial studies used polycrystalline ceramic particles, using single-crystalline particles would completely eliminate the high resistance grain boundary impedance component and would further improve the already high ionic conductance of these membranes. In an OPTM-Gen2 sample fabricated by the revised process the highest conductivities among OPTMs including previously reported ones were obtained. The conductivities are 0.53 mS/cm at 20 °C and 0.22 mS/cm at −10 °C, which are approximately 6 and 15 times higher, respectively, even in comparison with those of the commercial LATP sintered disc. The activation energy (17.2 kJ/mol) of OPTM-Gen2 is

consistent with that of the bulk (inner crystal) of LATP and it is approximately half that of

the commercial LATP sintered disc.

3.5   References

[1] Zhang J., Zhao N., Zhang M., Li Y., Chu P., Guo X., Di Z., Wang X., Li H., Nano Energy 28 (2016) 447–454.
[2] Liu W., Liu N., Sun J., Hsu P.C., Li Y., Lee H.W., Cui Y., Nano Lett. 15 (2015) 2740–2745.
[3] Zhai H., Xu P., Ning M., Cheng Q., Mandal J., Yang Y., Nano Lett. 17 (2017) 3182–3187.
[4] Choi W., Kim M., Park J.O., Kim J.H., Choi K., Kim Y.S., Kim T.Y., Ogata K., Im D., Doo S.G., Hwang Y., Sci. Rep. 7 (2017) 12037.
[5] Kiesow I., Marczewski D., Reinhardt L., Mühlmann M., Possiwan M., Goedel W. A., J. Am. Chem. Soc. 135 (2013), 4380.
[6] Schneider M., Schmidbauer W., Hochrein O., Pfeiffer T., Lauer S. (US Patent 20140057162 A1, 2014).
[7] Schmidbauer W., Roemer H., Raeke G.(US Patent 2004196887A, 2004)
[8] Irvine J. T. S., Sinclair D. C., West A. R., Adv. Mater. 2, 132 (1990).
[9] Minami T., Iwakura C., Kohjiya S., Tanaka I., Solid State Ionics for Batteries, Springer , Berlin 2006 .
[10] Hartmann P., Leichtweiss T., Busche M. R., Schneider M., Reich M., Sann J., Adelhelm P., Janek J., J. Phys. Chem. C 117 (2013) 21064.
[11] Sakamoto J., Rangasamy E., Kim H., Kim Y., Wolfenstine J., Nanotechnology 24 (2013) 424005 .
[12] Kamaya N., Homma K., Yamakawa Y., Hirayama M., Kanno R., Yonemura M., Kamiyama T., Kato Y., Hama S., Kawamoto K., Mitsui A., Nat. Mater.,10 (2011) 682 .
[13] Aetukuri N.B., Kitajima S., Jung E., Thompson L.E., Virwani K., Reich M.L., Kunze M., Schneider M., Schmidbauer W., Wilcke W.W., Bethune D.S., Scott J.C., Miller R.D., Kim H.-C., Adv. Energy Mater. 5 (2015) 1500265.
[14] Breuer S., Prutsch D., Ma Q., Epp V., Preishuber-Pflügl F., Tietz F., Wilkening M., J. Mater. Chem. A. 3 (2015) 21343–21350.
[15] Kotobuki M., Koishi M., Ceram. Int. 39 (2013) 4645–4649.

4 Batteries evaluations using the composite membranes

4.1 Introduction

OPTMs could display the high conductivity in chapter 3. Here, the discussions were divided into two parts; firstly, investigating the battery characteristics in OPTMs, and secondly the use of metallic Li as the anode material in terms of Li dendrite inhabitation. As a result, we succeeded in identifying the challenge and possibility of OPTMs.

Regarding the investigation of the battery characteristics in OPTMs fabricated under different conditions in the first discussion, the characteristics of OPTMs were clarified. Concretely speaking, by employing the electrode materials of the conventional LIBs, such as lithium titanate (LTO) as an anode material and lithium nickel-manganese-cobalt oxide (NMC) as a cathode material, the feasibility of using OPTMs in batteries were evaluated. LTO, especially, is well known for no dendrite formation on the surface of anode during cycling [1].

Secondly, the use of metallic Li as the anode material is a definitive route to increasing the energy density of state-of-the-art LIBs [2–6]. LIBs typically employ a Li-conducting liquid electrolyte and Li-intercalating electrode materials for the anode and cathode [7]. For a given cathode material, metallic Li maximizes the cell voltage and has a specific anode capacity nearly ten times larger than Li-intercalating graphitic anodes and therefore gives the maximum possible energy density of any anode material. In addition, to achieve the theoretically predicted high specific energy in Li–O_2 and Li–S batteries, the use

of metallic Li anodes is essential [9–12]. A significant barrier to the use of metallic Li anodes is the highly nonuniform electrochemical deposition of Li (during the recharge of these batteries) due to the formation and growth of needle-like crystals called dendrites [6,13–16]. Dendritic growth causes extreme roughening of the Li surface which can eventually short-circuit the cell and lead to catastrophic cell failure [2,6,15,17]. Both the surface tension of the electrolyte at the growing tip of the dendrite and the mechanical stress opposing its growth are known to inhibit the unfavorable roughening of the Li surface [13,14,18]. Efforts to tailor the surface tension of the electrolyte to inhibit dendritic growth and thereby promote smooth Li deposition have been unsuccessful [19]. An alternate approach is to mechanically suppress the growth of dendrites. A Li-ion-conducting electrode separator with a shear modulus at least twice that of Li ($G_{Li} \approx 3.4$ GPa) was predicted to be capable of suppressing dendritic growth by an opposing mechanical stress [13]. This modulus value of >6 GPa is difficult to achieve in an organic polymer without extensive cross-linking which embrittles the polymer [20]. LICC materials possess shear moduli much higher than the minimum required, and dendritic suppression in cells-employing LICC discs was experimentally demonstrated [6,21]. Most importantly OPTMs suppress Li dendrite growth because the spatial ionic current distribution in the membrane will favor dendrite growth exclusively toward the LICP which are able to resist dendrite penetration. There is no driving force for dendrite growth through the polymer matrix because it is a Li-ion insulator.

77

4.2   Experiments

4.2.1 Evaluation of the composite membranes employed batteries

$Li_4Ti_5O_{12}$ (LTO) powder (T30-D8, Posco ES Materials, Co., Ltd.), carbon black (Super-P, Erachem Comilog), and polyvinylidene fluoride (Solef-75130, Solvay, Co. Ltd.,) were dispersed in N-methyl-2-pyrrolidone (at 80:10:10 by weight) and mixed in a mixer for 2 h. The obtained slurry was coated on an Al foil current collector to obtain an electrode sheet and then dried in vacuum at 80 °C for 24 h. The active material loading of the anode was controlled to be about 6.0 mg cm^{-2}. The $LiNi_{1/3}Mn_{1/3}Co_{1/3}O_2$ (NMC) electrode (Umicore) was used as the cathode. The LTO/NMC coin cells with OPTMs were assembled in a dry room. As conventionally conducted, a liquid electrolyte was used to provide the Li-ion conduction to the positive and negative electrodes. The electrolyte of 1 M LiTFSI in a solvent of 20 : 80 w/w of 1,2-dimethoxyethane (Sigma-Aldrich Corp.) : 1,1,2,2-Tetrafluoroethyl 2,2,3,3-Tetrafluoropropyl Ether (SynQest Labs, Inc.) was retained in the Polyethelene (PE) separator (G1212A, Asahi Kasei Corp.). The battery tests with TOSCAT3100 (Toyo system) were performed in constant current and constant voltage mode. The cells were charged to 2.5 V at a current density and then kept at 2.5 V for 1 h. Then, the cells were discharged to 1.0 V at a current density. The current density was changed as follows: 0.1 mA cm^{-2} (1st cycle), 0.2 mA cm^{-2} (2nd cycle), and 0.6 mA cm^{-2} (more three cycles).

4.2.2 Structural and surface characterization

Scanning electron microscopy (SEM) images were obtained with a Nova^{TM} NanoSEM SEM (FEI Co. Ltd.). Specimens of OPTMs were prepared for cross-sectional imaging by IB-19520CCP, Cross Section polisher (JEOL Ltd.). X-ray photoelectron spectroscopy (XPS) analysis was performed using a Quantum2000 (ULVAC-PHI, Inc.). More detailed information is provided as the following section.

4.2.3 X-ray photoelectron spectroscopy (XPS) analysis

4.2.3.1 XPS - experimental details

The XPS testing was carried out using the Quantum2000 (ULVAC-PHI, Inc), which was outfitted with a monochromatic Al Kα X-ray source (1486.6 eV) for excitation. The electron energy analyzer was operated at a constant pass energy of 29.35 eV for XPS detail spectra and 187.85 eV for the survey spectra, respectively. During data acquisition, the samples were flooded with low kinetic energy electrons and Ar$^+$ ions in order to neutralize charging effects. The detail spectra were calibrated by 285.0 eV of C-C/C-H binding energy in C 1s signal.

4.3   Results and Discussion

4.3.1 Evaluation of the composite materials employed batteries

To evaluate the feasibility of using OPTMs in batteries, LTO/NMC cells with various OPTMs were assembled. Fig. 4-1 and Fig. 4-2 respectively show the initial

charge-discharge curves and the cycling performance of the LTO/NMC cells with various OPTMs in the voltage range of 1.0–2.5 V. The LTO/NMC cell with LP-RIE-0 (red) could not be activated at all even in the first cycle, because the etching side is completely covered with the insulating polymer. This demonstrates that the cathode and the anode are electrochemically separated in our cell construction. On the other hand, the other cells delivered each capacity and the cells using LP-RIE-120 and SP-RIE-40 can be cycled during more than 200 cycles. In terms of the overpotentials of the first charging, the values were observed in descending order as follows; LP-RIE-40 (green), LP-RIE-120 (blue) and SP-RIE-40 (purple). This is different tendency from those of the particle exposure area and impedance analysis. We estimate that this unexpected tendency was caused by the differences in the state of each surface. We therefore show XPS analysis data in Fig. 4-3, Fig. 4-4 and Fig. 4-5. These XPS data indicate the following two possibilities about surface impurities; (i) Polymer residues or degradation products (polymer derivatives) or (ii) the changes of LATP particle surfaces, as discussed details in the following section. Thus, we succeeded in preparing OPTM which achieves not only high energy/power density but also low overpotential by using smaller LATP particles and shorter O_2-RIE time. In addition, it was found that a challenge of OPTMs is to further decrease the cell overpotential. In order to achieve it, the investigation of a method of removing the surface impurities or generating no surface impurities through the process would be required.

80
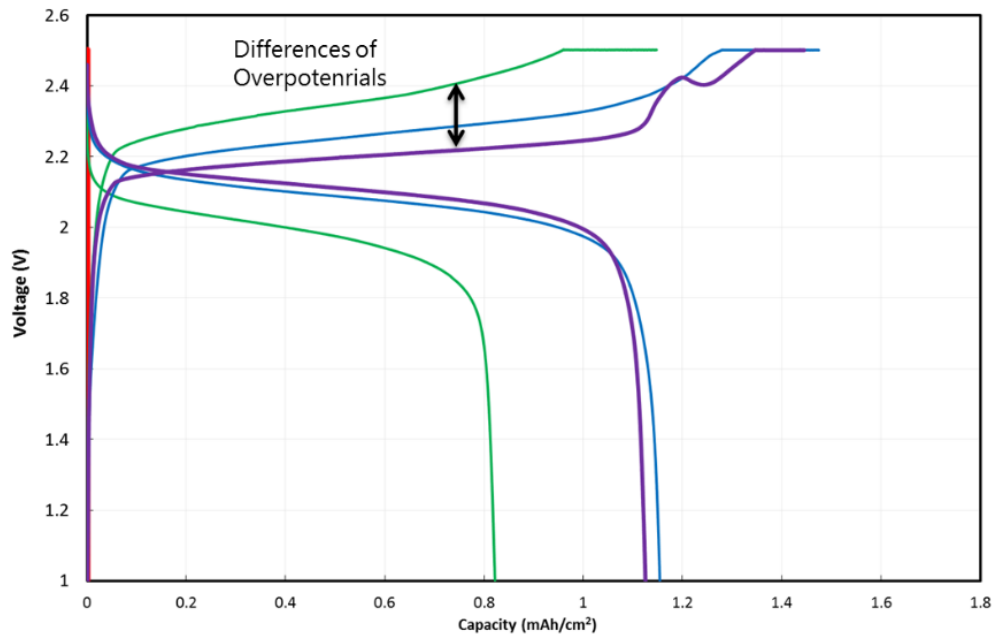
Fig. 4-1. Initial charge-discharge curves of LTO/NMC cells with various OPTMs.
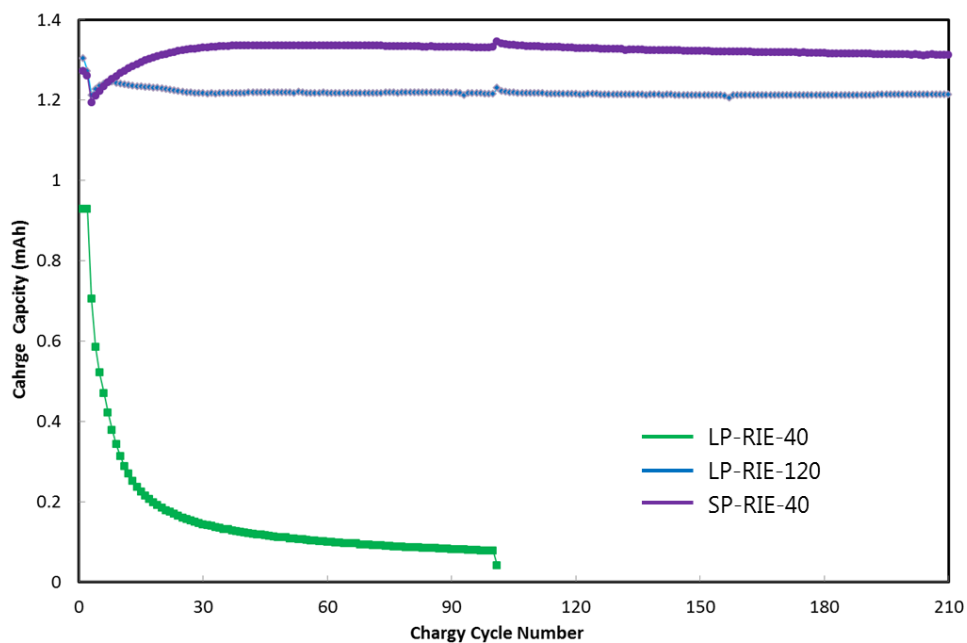
Fig. 4-2. Cycling performance of LTO/NMC cells with different OPTMs. The battery test with TOSCAT3100 (Toyo system) was performed in constant current and constant voltage mode. The cells were charged to 2.5 V at a current density and then kept at 2.5 V for 1h. Then the cells were discharged to 1.0 V at a current density. The current density was changed as follows: 0.1 mA/cm^2 (1st cycle), 0.2 mA/cm^2 (2nd cycle) and 0.6 mA/cm^2 (more than 3rd cycle).

4.3.2 XPS - detailed discussion

Fig. 4-3 shows wide-scan survey XPS results of the OPTM samples of LP-RIE-120and SP-RIE-40, and the pristine LATP particles. In the OPTMs, the polymer side was analyzed. The XPS sample of the pristine LATP particles was prepared by placing the pristine LATP particles on Kapton® tape. In all the samples, the signals for aluminum, lithium, titanium, phosphorous, oxygen and carbon from LATP particles and COP matrix (or Kapton® tape) were confirmed as expected. As mentioned above, the tendency of the magnitude of the overpotential is different from the tendency of the particle exposure and impedance analysis. Here, we demonstrate about two possibilities, which may resolve the above conflicting results, by using XPS detailed analysis.

(i) Polymer residues or degradation products (polymer derivatives)

Fig. 4-4 depicts XPS detail spectra of carbon (C 1s) for LP-RIE-120 and SP-RIE-40 before and after sputtering for 1 minute. In both the OPTM samples before sputtering, the C 1s signals around 284-289 eV were observed. The signals at 285 eV and 287 eV are mainly attributed to C-C/C-H of COP and C-O of PEO, respectively. After sputtering, the signals around 287 eV almost disappeared. This means that the surface of polymer side was contaminated by PEO used as the adhesive during process, but only a small amount of PEO remained in both the OPTM samples. Therefore, the residual PEO would not be the main factor of the conflicting results. On the other hand, the signals at 285 eV are remained in both samples after sputtering. However, about carbon concentration before and after

83

sputtering, LP-RIE-120 demonstrates the different change from SP-RIE-40. Table 4-1 shows the atomic concentration of each element related with LATP and COP for OPTM samples before and after sputtering. In SP-RIE-40, the ratio of carbon decreased after sputtering, whereas, in LP-RIE-120, the ratio of carbon after sputtering is almost the same as before sputtering. From these results, it is speculated that LP-RIE-120 has more polymer residues related with COP than SP-RIE-40. This speculation is supported by the SEM observation (Fig. 3-8 (c) and Fig. 3-14 (a) in chapter 3). The bristle brush-shaped structures were observed and LP-RIE-120 has longer shape than SP-RIE-40. If the residues are polymer derivatives, which have different properties from original COP such as solubility and electrochemical window, they would have a greater influence on the overpotential during battery tests than on the membrane resistance during Au/Au impedance measurements. Hence, LP-RIE-120 with a more polymer residues may have a larger overpotential than SP-RIE-40.

ii) Changes of LATP particle surfaces

There is a possibility that the changes of LATP particle surfaces were happened by O_2-RIE treatment in comparing with pristine LATP particles. The atomic concentration in Table 4-1 shows the non-stoichiometric composition of LATP in both the OPTM samples. The changes of chemical state of LATP are also observed in the XPS detailed analysis. Fig. 4-5 depicts XPS detail spectra of titanium (Ti $2p$) for LP-RIE-120 (before sputtering), SP-RIE-40 (before sputtering) and the pristine LATP particles. The Ti $2p$ signal of the

pristine LATP particles, which refers to binding energies of 466.0/460.2 eV (attributed to Ti $2p_{1/2}$/Ti $2p_{3/2}$, respectively), can be assigned to Ti^{4+} of LATP [22-24]. However, both the Ti peaks of LP-RIE-120 and SP-RIE-40 shifted to 465.0/458.9 eV and 465.2/459.6 eV, respectively. It is reported that the peak shift to the lower binding energy was caused by a change in oxidation state to Ti^{3+}, and reduced LATP shows lower ionic conductivity and higher electronic conductivity than original LATP [22,23]. In the case that reduced LATP layer has higher electronic conductivity than ionic conductivity, the resistance measured in the Au/Au cell includes the resistance depending on the electronic conductivity of reduced LATP layer. On the other hand, the overpotential during battery tests is influenced by the ionic conductivity of reduced LATP layer. Therefore, the conflicting results can be explained when certain conditions about thickness, ionic conductivity and electronic conductivity of the reduced LATP layer are met.
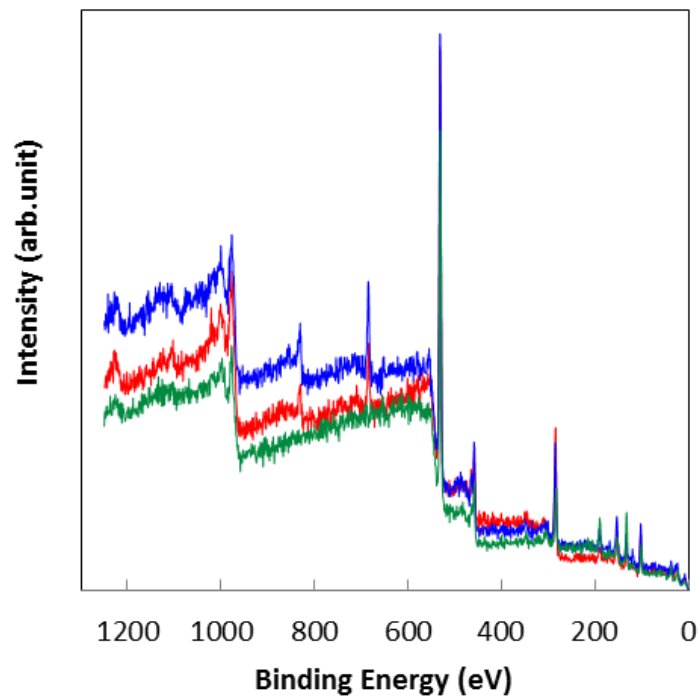
Fig. 4-3. Wide-scan survey XPS spectra of LP-RIE-120 (red), SP-RIE-40 (blue) and the pristine LATP (green)

Table 4-1. XPS atomic concentration quantification on the surface of LP-RIE-120 and SP-RIE-40

	Li 1s	C 1s	O 1s	Al 2p	P 2p	Ti 2p
LP-RIE-120 (before sputtering)	6.42	40.27	47.10	0.29	2.58	3.34
SP-RIE-40 (before sputtering)	7.30	30.29	53.08	1.33	3.76	4.24
LP-RIE-120 (after sputtering)	6.95	40.75	41.06	1.59	4.42	5.22
SP-RIE-40 (after sputtering)	2.99	19.53	60.56	2.40	6.98	7.53

Fig. 4-4. Detailed XPS spectra of carbon (C 1s); LP-RIE-120 (before sputtering; red, and after sputtering; green) and SP-RIE-40 (before sputtering; blue, and after sputtering; orange)
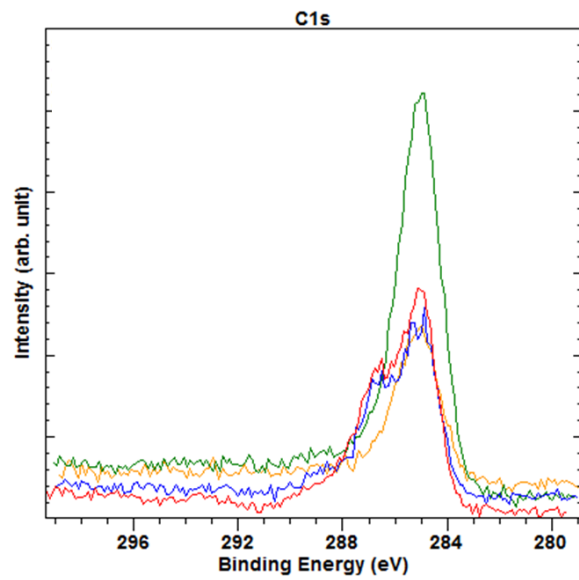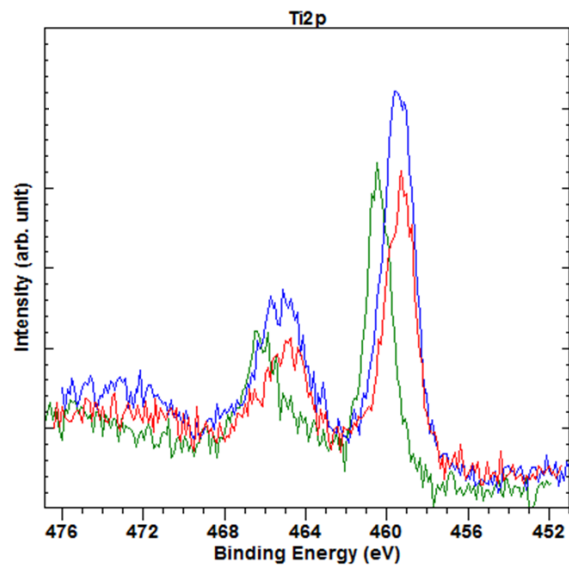
Fig. 4-5. Detailed XPS spectra of titanium (Ti 2*p*); LP-RIE-120 (red), SP-RIE-40 (blue) and the pristine LATP (green)

4.4 Li metal anode

A particularly important criterion for the usefulness of Li-ion-conducting membranes in battery applications is their ability to resist dendrite penetration, especially for use of Li metal anode. A Li-ion-conducting electrode separator with a shear modulus at least twice that of Li (G Li ≈3.4 GPa) was predicted to be capable of suppressing dendritic growth by an opposing mechanical stress [13]. This modulus value of >6 GPa is difficult to achieve in an organic polymer without extensive cross-linking which embrittles the polymer [20] LICC materials possess shear moduli much higher than the minimum required, and dendritic suppression in cells-employing LICC discs was experimentally demonstrated [6,21].

4.4.1 Dendrite growth experiments

To test the penetration resistance of the membrane separator to dendrite formation, a planar lithium-lithium (Li-Li) symmetric cell, which is a specially designed cell with optical ports that allow in operando optical imaging, is developed. Dendrite growth is monitored in cells with either a Celgard 2500 separator (a commonly used porous separator in LIBs) or the OPTM-Gen1, placed next to the cathodic Li electrode(Fig. 4-6 and Fig. 4-7). A constant current of 1.5 mA was applied to motivate dendritic growth on the surface of the cathodic Li electrode. Quartz windows on the cell allowed for in-situ optical imaging of the dendritic growth of Li. 1 M bis(trifl uoromethane sulfonyl)imide (LiTFSI) in 1,2-dimethoxyethane (DME) liquid electrolyte is used in both cases. A current of 1.5 mA

(current density $\approx$6 mA/cm^2) was applied to promote Li deposition on the cathodic Li electrode. In the cell employing Celgard 2500, dendritic growth was clearly noticeable within a minute of the application of the current (Fig. 4-7). Dendrites grew rapidly in this cell, extending through the pores in the separator and finally causing cell failure in less than $\approx$6 min time. In stark contrast, there was no evidence of dendritic growth when the OPTMs were employed as separators in a similar cell. This was true even after the passage of current for $\approx$40 min. Even though the membranes have a soft polymer matrix ($G^{COP} < 3$ GPa), the remarkable dendritic growth suppression with these membranes is not unexpected, for the following reasons. First, the LICPs are known to have high enough shear moduli (>20 GPa) and the ability to mechanically suppress dendritic growth. Second, since the polymer matrix is not a Li-ion conductor, there is no ionic current through the polymer matrix to provide the driving force for dendritic growth perpendicular to the matrix plane. Hence, the dendrites do not grow through the Li-ion insulating polymer matrix even though it has a lower modulus than Li ($G^{Li} \approx 3.4$ GPa). In addition to the high shear modulus of the ceramic particles, the Li-ion insulating nature of the polymer matrix is therefore critical for dendritic growth suppression in these OPTMs. A very important implication is that the modulus of the matrix is irrelevant for preventing dendritic growth through the membranes if it has no Li-ion conductivity. This allows the choice of any material with suitable thermomechanical properties, high chemical and electrochemical stability, and good interfacial adhesion to the ceramic particles, without any restriction on its modulus.
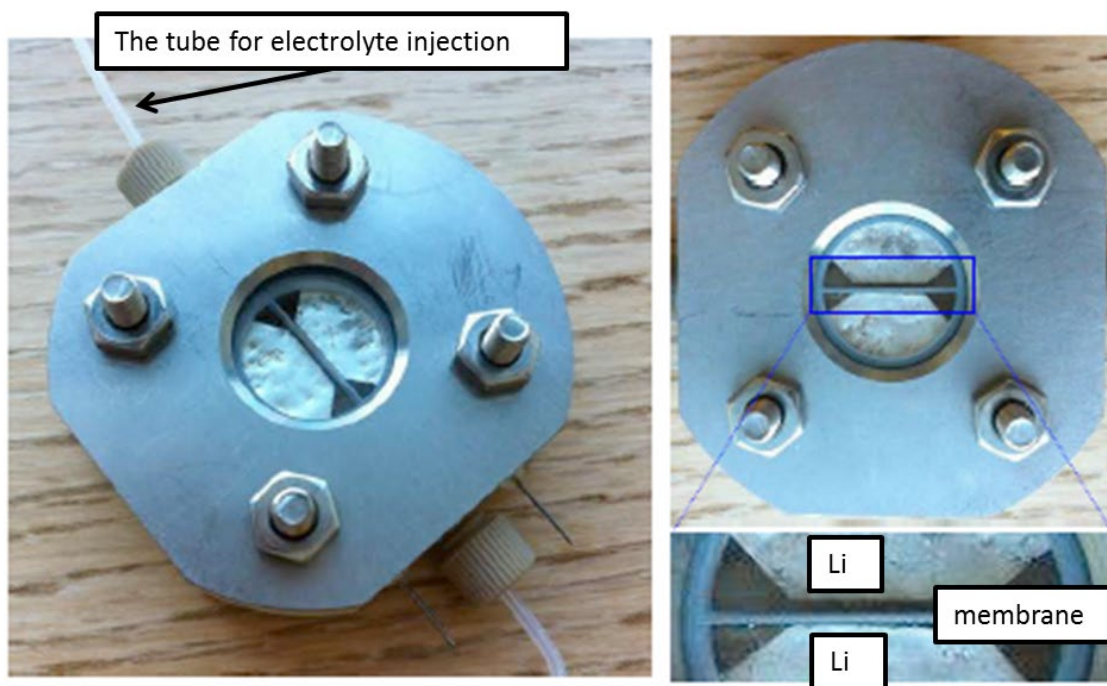
Fig. 4-6. Optical photographs of the observational cell used for dendrite growth experiments. a) Photograph of the full assembled cell. The two electrode pins and the tubes for electrolyte injection can be seen. b) A front-view of the same cell and c) a zoomed-in picture showing the two Li electrodes (L) and a central slot for placing the separator (S). This is the view seen through the microscope used for capturing the images shown in Fig. 4-7. For scale, the diameter of the quartz window is 17 mm.
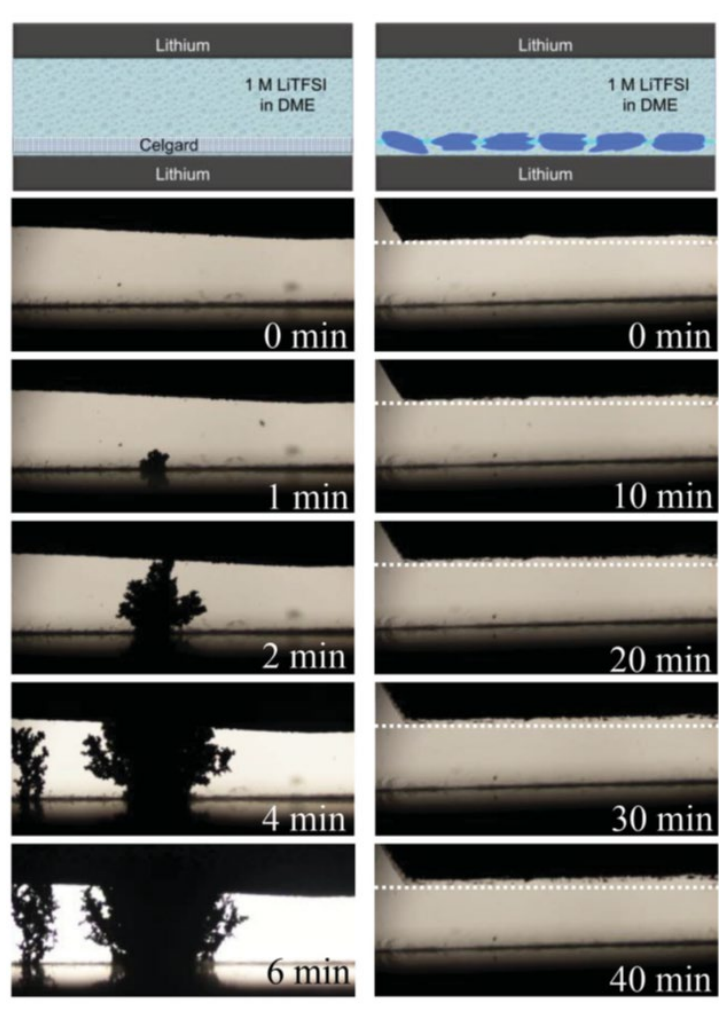
Fig. 4-7. Optical images of dendrite growth in a custom built symmetric Li-Li cell. The experimental arrangement is shown schematically in the top two panels. Li dendritic growth, observed with the celgard separator, is completely suppressed by using the OPTM developed in this work. The white dotted line in the images with the OPTM shows the approximate position of the surface of the dissolving Li electrode, at the beginning of the experiment. Clearly, Li at this electrode dissolves after the application of a discharge current of 1.5 mA, but dendrites do not grow through the composite membrane as Li deposits on the cathodic Li electrode. The width of the images is ≈3 mm

4.4.2 Interface Characterization by Nanoindentation measurements

The optical images shown in Fig. 4-7 also suggest that there is no dendritic growth along the interfaces between the ceramic particles and the polymer matrix. This suggests that there is adequate adhesion at the ceramic–polymer interface, which can be quantified by nanoindentation measurements [25,26]. Nanoindentation measurements are performed on a Hysitron Triboindenter 950 system with a PerforMech controller using a NorthStar cube corner probe with an end radius of ~35 nm. Prior to measurements, calibrations are performed on fused silica. For nanoindentation measurements, the OPTM is glued onto a stainless steel puck with a cyano-acrylate based super-glue. Extreme care is taken to ensure that the glue does not flow to the top of the membrane. The sample, on the stainless steel puck, is magnetically attached to the sample stage. Load displacement curves, are obtained by measuring displacement as a function of increasing and decreasing load in the range of 0-10 μN. Curves, with a lateral separation of 1.5 μm, are obtained to cover a square grid area of 43.5 x 43.5 μm2 on the OPTM. The probe locates the surface with a set-point of 700 nN. For each indent the probe and the sample equilibrate for a total of 2 min and an average drift (usually < 0.05 nm/s) measured during the equilibration time is automatically corrected. The maximum indentation depths are <120 nm. The measured load displacement curves are manually offset to give zero displacement in the no load condition and fitted to the unload portion of the load-displacement curves using an automated curve-fit function to extract the indentation modulus plotted in Fig. 4-8. Moreover, as shown in Fig. 4-9, the curves are representative of the three different regions observable in the 2D modulus plot of

94

Fig. 4-8. Typical load-displacement curves were obtained by these nano indentation measurements on the ceramic particle (red), and on the polymer matrix near the polymer-ceramic interface region (cyan) and further away from the interface (blue). The indentation modulus values (Er) obtained by curve fitting to the unload portion of the curve are also given. As the results, if the polymer–ceramic adhesion is poor, a decreased indentation modulus would be expected near the interface. However, these measurements show that the transition at the interface is nearly abrupt, with no decrease in the modulus of the polymer matrix near the interface. Remarkably, there is an increase in the moduli of the polymer matrix near the interface with the ceramic particle, which is due to a resistance to strain propagation near the particle. This is only possible if there is good interfacial bonding.

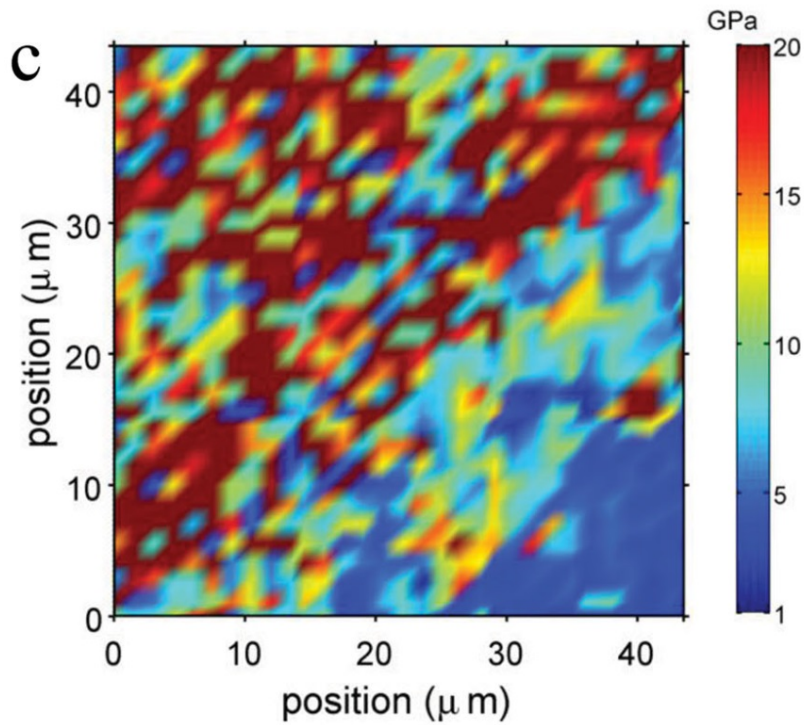Fig. 4-8. A 2D map of indentation modulus for the OPTM showing that the polymer near the interface (light blue colored band) has modulus values between those of the ceramic particle (predominantly red colored region) and the polymer more distant from the interface (predominantly blue colored bottom right corner). This is interpreted as indirect evidence for substantial interfacial bonding between COP and ceramic particles.
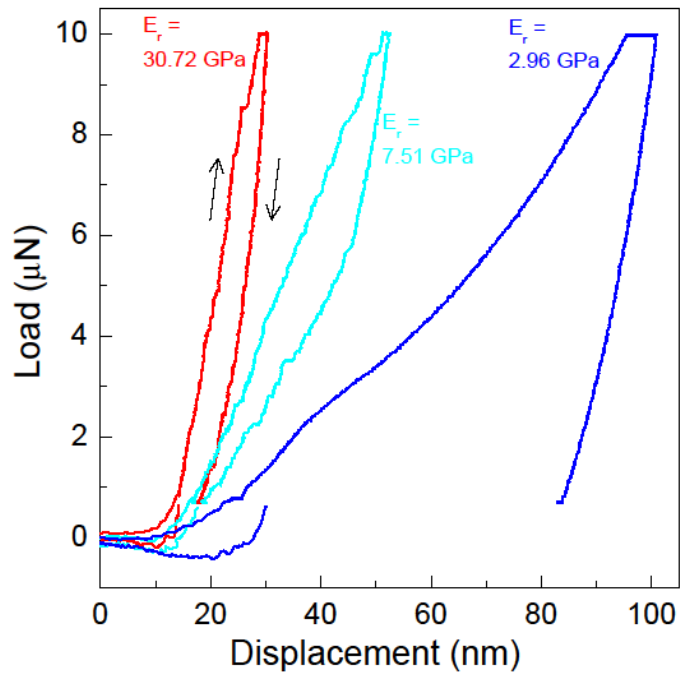
Fig. 4-9. Typical load-displacement curves obtained by nano indentation measurements on the ceramic particle (red), and on the polymer matrix near the polymer-ceramic interface region (cyan) and further away from the interface (blue). The indentation modulus values (Er) obtained by curve fitting to the unload portion of the curve are also given. These curves are representative of the three different regions observable in the 2D modulus plot of Fig. 4-8.

4.5 Conclusion

Thinner OPTM provided the high energy/power density and low overpotential in batteries. Evaluation of the cell performance indicated that the overpotential, which may be caused by surface issues, is a challenge to using OPTMs. We believe that overcoming the surface issues will enable reduction of overpotential and thus, practical use of OPTMs in the batteries.

Notably, these membranes resist the penetration of Li dendrites. Our work demonstrates that the polymer matrix modulus can be quite low and still resist dendrite penetration as long as it forms a strong interface with the particles and is not itself a Li-ion conductor. We succeeded in identifying the challenge and possibility of OPTMs.

4.6   References

[1] Ohzuku T., Ueda A., Yamamoto N., J. Electrochem. Soc. 142, 1431–1435 (1995).

[2] Zheng G., Lee S. W., Liang Z., Lee H.-W., Yan K., Yao, Wang H., Li W., Chu S., Cui Y., Nat. Nanotechnol. 9 (2014) 618.

[3] Goodenough J. B., Park K.-S., J. Am. Chem. Soc. 2013 , 135 , 1167 .

[4] Bouchet R., Nat. Nanotechnol. 9 (2014) 572 .

[5] Aurbach D., Pollak E., Elazari R., Salitra G., Kelley C. S., Affinito J., J. Electrochem. Soc.156 (2009) A694 .

[6] Z. Li , J. Huang , B. Yann Liaw , V. Metzler , J. Zhang , J. Power Sources 254 (2014) 168 .

[7] Tarascon J. M., Armand M. Nature 414 (2001) 359 .

[8] Bruce P. G., Freunberger S. A., Hardwick L. J., Tarascon J.-M. Nat. Mater. 2012 , 11 , 19 .

[9] Lithium Air Batteries: Fundamentals (Eds: Imanishi N., Luntz A. C., Bruce P.), Springer , New York 2014 .

[10] Christensen J., Albertus P., Sanchez-Carrera R. S., Lohmann T., Kozinsky B., Liedtke R., Ahmed J., Kojic A., J. Electrochem. Soc. 2011 , 159 , R1 .

[11] Peng Z., Freunberger S. A., Chen Y., Bruce P. G., Science 2012 , 337 , 563.

[12] Aetukuri N. B., McCloskey B. D., García J. M., Krupp L. E., Viswanathan V., Luntz A. C., Nat. Chem. 7 (2015) 50 .

[13] Monroe C., Newman J., J. Electrochem. Soc. 152 (2015) A396 .

[14] Monroe C., Newman J., J. Electrochem. Soc. 150 (2003) A1377 .

[15] Harry K. J., Hallinan D. T., Parkinson D. Y., MacDowell A. A., Balsara N. P., Nat. Mater. 13 (2014) 69 .

[16] Barkey D., Oberholtzer F., Wu Q., Phys. Rev. Lett. 1995 , 75 (1995) 2980.

[17] Newman J. E., Thomas-Alyea K. E., Electrochemical Systems, Wiley Interscience, New York 2004 .

[18] Sundström L.-G., Bark F. H., Electrochim. Acta 40 (1995) 599.

[19] Stone G. M., Mullin S. A., Teran A. A., Hallinan D. T., Minor A. M., Hexemer A., Balsara N. P., J. Electrochem. Soc. 159 (2012) A222.

[20] Landel R. F., Nielsen L. E., Mechanical Properties of Polymers and Composites , Taylor and Francis , London 1993 .

[21] Thangadurai V., Narayanan S., Pinzaru D., Chem. Soc. Rev. 43 (2014) 4714.

[22] Wang S., Ding Y., Zhou G., Yu G., Manthiram A., ACS Energy Lett. 1 (2016) 1080–1085. doi:10.1021/acsenergylett.6b00481.

[23] Busche M.R., Drossel T., Leichtweiss T., Weber D.A., Falk M., Schneider M., Reich M.L. Sommer, H., Adelhelm P., Janek J., Nat. Chem. 8 (2016) 426–434. doi:10.1038/nchem.2470.

[24] Deng Y.F., Zhao S.X., Xu Y.H., Nan C.W., J. Power Sources. 296 (2015) 261–267.

[25] Hodzic A., Stachurski Z. H., Kim J. K, Polymer 41 (2000) 6895.

[26] Fischer-Cripps A. C., Nanoindentation , Springer , Berlin 2002.

5 Conclusions and outlook

In this dissertation, the results have been divided into three chapters and a summary regarding the findings of this study. This chapter summarizes my research intentions, are technical summary of every finding, and a brief outlook toward the application of this research.

5.1 Conclusions

The present dissertation deals with the newly designed polymer/inorganic composite electrolytes as well as processing techniques for producing a future-generation all-solid-state battery of high power density, high energy density, and superior safety.

Chapter 2 presents the newly designed CLs, which are applicable to large-scale production of composite materials. In addition, we investigated the Li-ion transfer mechanism by using AC impedance spectroscopy measurements. CL-LATP exhibited a high conductivity of 0.14 mS/cm at room temperature. We demonstrated, in chapter 3, a simple route for fabricating flexible Li-ion-conducting OPTMs with high Li-ion conductance and significantly improved mechanical properties relative to LICC discs of comparable thickness. This configuration eliminates the highly resistive interparticle ionic conduction pathways that are characteristic of multiparticle thick composites. Moreover, the conductivities were 0.53 mS/cm at 20 °C and 0.22 mS/cm at −10 °C, which are ~6 and 15 times higher, respectively, even in comparison with those of the commercial LATP sintered disc. The activation energy (17.2 kJ/mol) of OPTMs is consistent with that of the

bulk (inner crystal) of LATP and is approximately half of the commercial LATP sintered disc. In chapter 4, we discussed the successful fabrication of a thinner OPTM, which provides high energy/power density and low overpotential in batteries. Finally, the evaluation of the cell performance clarified a challenge of overpotential, which may be caused by the surface issues of OPTMs. We believe that the solution of the surface issues will lead to the reduction in overpotential and realize the practical use of OPTMs in the batteries. Furthermore, we demonstrated that the polymer matrix of the modulus, at OPTMs, can be considerably low and still resist dendrite penetration as long as it forms a strong interface with the particles and is not itself a Li-ion conductor.

5.2   Outlook

Compact, safe, high-capacity rechargeable batteries with longer cycling life are pivotal to the development of lightweight portable electronics, electrification of transportation, and for the storage and utilization of renewable energy. To heat up competition in the growing battery industry, the development of all-solid-state LIBs is an attractive option. Through this dissertation, the proposed novel designed composite membranes are shown to have some potential practical applications, as a part of solid electrolytes, to all-solid-state LIBs because of their features such as low resistance, flexibility, and toughness against Li dendrite growth. These advantages may impart thinness, flexibility, and plausible application as the Li metal anode to the batteries produced with the proposed composite membranes.

6 Acknowledgements

I express my sincere gratitude and appreciation to various individuals who helped me improve this dissertation. First, I express my special appreciation and gratitude to my advisors Prof. Haoshen Zhou (AIST and University of Tsukuba) and Dr. Hirokazu Kitaura (AIST) for their patience and valuable discussions regarding the details of this dissertation. I am very grateful for the great opportunity that University of Tsukuba has offered in order for me to evolve as a scientist and to conduct my experimentation. In particular, I appreciate Prof. Masayoshi Ishida for his authentic guidance and Prof. Hirohisa Aki and Prof. Keiichi Okajima for their useful advice.

This research was initially started at the IBM Almaden Research Center in San Jose, United States of America, under the membership of the IBM 500 project during my tenure with Asahi Kasei Corp., where this company sent me for this project. I'm thankful for this business relationship with the company and all project members for their help. I would like to particularly thank the precious supporters of Asahi Kasei Corp.—Dr. Shigeki Takayama, Dr. Akira Yoshino, Dr. Yoshiyuki Ishii, Mr. Kenichiro Iwamura, and Mr. Yasushi Kaneko and those of IBM Corp.—Dr. Ho-Cheol Kim, Dr. Robert Miller (former employee), and Prof. Bryan D. McCloskey (former employee). Furthermore, I wish to acknowledge Samsung Electronics Corp. for giving me the opportunity to pursue my academic education. I am particularly grateful to Dr. Yunil Hwan (former employee) and Dr. Dongmin Im. Apart from these, I would also like to thank all not only the members of University of Tsukuba

and AIST but also my colleagues at Asahi Kasei Corp., IBM Corp., and Samsung Electronics Corp.

Finally and most importantly, I would like to thank my parents, Yoshihisa and Hiroko Kitajima, for all the motivational expectations as well as my sister, Kanako Takei. In addition, I would like to thank my wife, Sanae Kitajima, and my children, Yuna and Haruki, for their love and support. These people have motivated me to pursue my dream of contributing to the research and development field of Material Science. Lastly, I would like to thank my entire family for their continuous encouragement and reliable support.

Shintaro Kitajima

March 2019

7 List of publications

This dissertation comprises a summary based on the following papers;

[1] Fabrication and impedance analysis for designed composite layers with polymer and inorganic electrolytes leading to high conductivity
Shintaro Kitajima, Hirokazu Kitaura,, Dongmin Im, Yunil Hwang, Masayoshi Ishida, Haoshen Zhou, Solid State Ionics, 316 (2018) 29-33

[2] Flexible ion-conducting composite membranes for lithium batteries,
*Nagaphani B. Aetukuri,*Shintaro Kitajima, Edward Jung, Leslie E. Thompson , Kumar Virwani, Maria-Louisa Reich, Miriam Kunze, Meike Schneider, Wolfgang Schmidbauer, Winfried W. Wilcke, Donald S. Bethune, J. Campbell Scott, Robert D. Miller, and Ho-Cheol Kim, Adv. Energy Mater. 5 (2015) 1500265 (*These authors contributed equally to this work)

[3] Hybridizing monolayered inorganic electrolytes and polymer for high conductivity and low activation energy in Li-ion batteries,
Shintaro Kitajima, Hirokazu Kitaura, Wonsung Choi, Toshinori Sugimoto, Youngeal Kim, Kieyoung Woo, Won-seok Chang, Hyunseok Kim, Yong-Gun Lee, Jusik Kim, Jaegwan Chung, Jaecheol Lee, WoonJoong Baek, Yong-Hoon Cho, Dongmin Im, Seok Gwang Doo, Masayoshi Ishida, Haoshen Zhou, Solid State Ionics (submitted)

The following paper is not included in this dissertation;

[4] Growth mechanism and inhibition technologies of a contamination on the surface of photomask for longtime,
Makoto Murai, Masayoshi Tsuchiya, Hiroyuki Shinchi, and Terumasa Hirano, Shintaro Kitajima, Yasushi Kaneko, Takahisa Kimoto, and Shigeki Takayama, Proc. SPIE 8081, 808105 (2011)